

1 Statistical Analysis of Contrail to Cirrus Evolution during the Contrail and Cirrus Experiments
2 (CONCERT)

3 Aurélien Chauvigné¹, Olivier Jourdan¹, Alfons Schwarzenboeck¹, Christophe Gourbeyre¹, Jean
4 François Gayet¹, Christiane Voigt^{2,3}, Hans Schlager², Stefan Kaufmann², Stephan Borrmann^{3,4},
5 Sergej Molleker^{3,4}, Andreas Minikin^{2,5}, Tina Jurkat², Ulrich Schumann²

6 ¹Laboratoire de Météorologie Physique, UMR 6016 CNRS/Université Clermont Auvergne,
7 Clermont-Ferrand, France.

8 ²Institut für Physik der Atmosphäre, Deutsches Zentrum für Luft- und Raumfahrt (DLR),
9 Oberpfaffenhofen, Germany.

10 ³Institut für Physik der Atmosphäre, Universität Mainz, Mainz, Germany.

11 ⁴Max-Planck-Institute for Chemistry, Department for Particle Chemistry, Mainz, Germany.

12 ⁵Now at: Flugexperimente, Deutsches Zentrum für Luft- und Raumfahrt (DLR), Oberpfaffenhofen,
13 Germany.

14 **Abstract:**

15 Air traffic affects the cloudiness, and thus the climate, by emitting exhaust gases and particles.
16 The study of the evolution of contrail properties is very challenging due to the complex interplay of
17 vortex dynamics and atmospheric environment (e.g. temperature, supersaturation). Despite
18 substantial progress in recent years, the optical, microphysical, and macrophysical properties of
19 contrails and ambient cirrus during contrail formation and subsequent ageing are still subject to large
20 uncertainties due to instrumental and observational limitations and the large number of variables
21 influencing the contrail life cycle. In this study, various contrail cases corresponding to different
22 aircraft types and atmospheric conditions are investigated using a statistical method based on the in
23 situ optical measurements performed during the CONCERT campaigns 2008 and 2011. These two
24 aircraft campaigns encompass more than 17 aircraft contrail cases. A Principal Component Analysis
25 (PCA) of the angular scattering coefficients measured by the Polar Nephelometer is implemented.
26 The goal is to classify the sampled ice cloud measurements in 6 clusters representative of different
27 contrail development stages (primary wake, young contrail, contrail-cirrus and cirrus). Extinction
28 and, asymmetry coefficients, nitrogen oxide concentrations, relative humidity with respect to ice
29 (RHI) and particle size distributions are analysed for each cluster to characterize the evolution of ice-
30 cloud properties during the contrail to cirrus evolution. The PCA demonstrates that contrail optical
31 properties are well suited to identify and discriminate the different contrail growth stages and to
32 characterize the evolution of contrail properties.

33 **1 Introduction**

34 Aircraft exhaust plumes have a significant impact on climate and tropospheric chemistry (Lee
35 et al., 2010; IPCC, 1999). The Intergovernmental Panel for Climate Change IPCC special report on
36 aviation (1999) estimates that NO_x emissions from subsonic aircraft increase ozone concentrations at
37 cruise level. Short and long lived pollution species have different impact on atmospheric chemical
38 composition depending on the flight level (Frömming et al, 2012). Emissions of water vapour, black
39 carbon (BC) / soot particles, sulphate (SO₄) aerosols and nitrogen oxides (NO_x) contribute to the
40 modification of the chemical composition of the upper troposphere on shorter timescales (Lee et al.,
41 2010, Gettelman and Chen, 2013; Liou et al., 2013). The long-term climate impact is mainly driven
42 by CO₂ emissions. Modelling studies have shown that the direct radiative forcing from aviation is
43 expected to represent 3-4% (50-60 mW m⁻²) of the anthropogenic forcing (Lee et al., 2010; De Leon

44 et al., 2012) and could reach 87 mW m^{-2} in 2025 (Chen and Gettelman, 2016). Aircraft induced
45 cloudiness has also an important impact on climate, although the quantitative assessment of the
46 radiative forcing remains a major source of uncertainties (Lee et al., 2010).

47 1.1. Contrail formation and evolution

48 Contrail formation is mainly controlled by the thermodynamic properties of the ambient air
49 and by the aircraft emissions. The conditions for contrail formation can be determined by the Schmidt-
50 Appleman Criterion (SAC) (Schumann, 1996). Contrail chemical composition can have a significant
51 impact on the contrail formation (Kärcher et al., 2009). Indeed, the contrail microphysical properties,
52 as the total number densities and ice crystal diameters, are directly linked to the emission index (e.g.
53 soot emission index in kg-fuel^{-1}). Several studies in the past have been dedicated to the evolution of
54 concentrations of nitrogen oxide (NO) and sulphur dioxide (SO₂) and their oxidized forms (Kärcher
55 and Voigt, 2006 ; Voigt et al., 2006 ; Schäuble et al., 2009 ; Jurkat et al., 2011).

56 Two different processes of contrail formation have been studied: combustion condensation
57 trails and aerodynamic condensation trails. Different studies (Gierens and Dilger, 2013; Jansen and
58 Heymsfield, 2015) have illustrated characteristics of aerodynamically controlled contrail formation
59 associated to warmer temperatures (observations at temperatures above -38°C). Contrails primarily
60 initiated by the combustion processes result from the mixing of hot and humid exhaust gases with
61 cooler and dryer ambient air. This increases the local relative humidity in the exhaust plume leading
62 to the formation of contrails when the saturation with respect to liquid water is reached. In this case,
63 soot and sulphate aerosols emitted by the aircraft (Moore et al., 2017) may act as condensation nuclei
64 to form liquid droplets. Homogeneous ice nucleation of the liquid droplets can occur when the exhaust
65 cools down through mixing with the ambient temperature, while preserving ice saturation. Small ice
66 crystals are then formed in the jet phase within some tenths of a second (Kaercher and Yu, 2009).

67 The life-cycle of contrails depends on the interaction with the wake vortices behind aircraft
68 and the ambient atmosphere (Irvine et al., 2012; Graf et al., 2012; Duda et al., 2013; Carleton et al.,
69 2013; Schumann and Heymsfield, 2017). The ice crystals in the young contrails are captured within
70 two counter-rotating wake vortices in the downwash behind the aircraft induced by the aircraft lift,
71 which induce adiabatic compression, heating, and partial sublimation of the ice crystals within the
72 primary wake (Lewellen and Lewellen, 2001; Sussmann and Gierens, 2001, Unterstrasser et al., 2008,
73 Unterstrasser et al., 2016; Kärcher and Voigt, 2017). This primary wake may soon disappear if
74 ambient air is subsaturated with respect to ice. In the case of supersaturation, the secondary wake
75 becomes visible, thereby detraining ice particles from the primary wake at a higher level (Sussmann
76 and Gierens, 1999, Kaufmann et al., 2014). Quasi spherical ice crystals become increasingly
77 aspherical and grow by uptake of water vapour as long as saturation with respect to ice is prevailing.
78 In ice saturated conditions, contrails can persist after the vortex breakdown, spread and evolve into
79 contrail cirrus (Schumann and Heymsfield, 2017). The associated cloud cover (larger than for linear
80 contrails alone) increases the radiative forcing of contrail cirrus (Burkhardt and Kärcher, 2011;
81 Schumann et al., 2015).

82 1.2. Optical and microphysical properties of contrail phases

83 The assessment of the contrail radiative forcing requires, in particular, an accurate estimation
84 of the cloud cover, the visible optical depth, the single scattering characteristics, the ice crystal
85 effective size and habit (Yang et al., 2010; Spangenberg et al., 2013). Satellite observations provide
86 a comprehensive dataset to study statistically the contrail to cirrus evolution. The combined contrail
87 tracking algorithms on the Spinning Enhanced Visible and Infrared Imager (SEVIRI) on board the
88 Meteosat Second Generation (MSG) satellites with properties inferred by the Moderate Imaging

89 Spectroradiometer (MODIS) on board the Terra satellite was used by Vazquez-Navarro et al., (2015)
90 to characterize the properties of 2300 contrails. Properties included lifetime (mean values of 1h), the
91 length (130 km), the optical thickness (0.34), the altitude (11.7 km) and the radiative forcing (-26 W
92 m^{-2} for shortwave forcing over land) of these contrails.

93 However, detailed in situ optical and microphysical measurements are still needed to evaluate
94 satellite products and to develop more appropriate retrieval algorithm. Discriminating contrails from
95 natural cirrus from satellite observations remains extremely challenging. Although the optical and
96 microphysical properties of young contrails (linear contrails) differ from natural cirrus properties, the
97 contrail properties are highly time dependent and persistent contrail cirrus can be embedded in thin
98 cirrus clouds. Recent *in situ* measurements (Voigt et al., 2017) show that the microphysical properties
99 of contrail cirrus can still be distinguished from natural cirrus at contrail cirrus ages up to several
100 hours.

101 Most of the studies (Jessberger et al., 2013; Lewellen et al., 2012 ; Schumann et al., 2013)
102 separate the contrail analysis between the two wakes. Primary and secondary wake properties depend
103 strongly on atmospheric conditions and aircraft type (emission index, vortex, flight level, ambient
104 humidity, temperature, ...). In the primary wake, contrail ice crystals are quasi-spherical with values
105 of the effective diameter (D_{eff}) typically lower than $4 \mu\text{m}$ (Schumann et al., 2011; Gayet et al., 2012;
106 Järvinen et al., 2016; Schumann et al., 2017b). The total number concentration of ice particles is
107 typically larger than 1000 cm^{-3} a few seconds after contrail formation (Baumgardner and Gandrud,
108 1998; Petzold et al., 1997). Then, it decreases by dilution to concentrations below 200 cm^{-3} within
109 less than a minute after contrail generation (Poellot et al., 1999; Schröder et al., 2000; Gayet et al.,
110 2012). Gayet et al. (2012) reported mean values of ice water content of 3 mg m^{-3} and maximum
111 extinction coefficients close to 7 km^{-1} . In agreement with these results, the recent overview on contrail
112 studies presented in Schumann et al. (2017b) reports several microphysical properties at different
113 stages, for different atmospheric conditions as well as comparisons with the Contrail Cirrus Prediction
114 (CoCIP) model simulations. Their study also highlights a large variability (which increases with
115 contrail age) of contrail properties.

116 Several studies reported findings on the secondary wake and its evolution into contrail cirrus.
117 Detained from the primary wake and submitted to saturated ambient air with respect to ice, ice
118 crystals grow rapidly, while crystal concentration decreases. Within the first minutes after formation,
119 measurements exhibit aspherical ice crystals characterized by effective sizes up to $6 \mu\text{m}$, IWC ranging
120 between 2.5 and 10 mg m^{-3} , extinction between 2 and 3 km^{-1} , with crystal concentrations typically
121 lower than 100 cm^{-3} (Goodman et al., 1998; Voigt et al., 2010; Kübbeler et al., 2011; Gayet et al.,
122 2012; Jeßberger et al., 2013; Schumann et al., 2013; Poellot et al., 1999; Febvre et al., 2009;
123 Kaufmann et al., 2014). Aged contrails can persist and evolve into contrail cirrus if the ambient air is
124 saturated with respect to ice, however those studies are limited by the lack of unambiguous
125 identification (Schumann et al., 2017a).

126 After a few minutes, tracking contrails by visual navigation is challenging as contrail and
127 contrail cirrus spread in the free troposphere. Observations of the ice crystal shape and growth over
128 several tens of minutes and up to an hour illustrate that crystal effective size can easily reach $20 \mu\text{m}$
129 and beyond with number concentrations ranging from 1 to 5 cm^{-3} (Lawson et al., 1998; Schäuble et
130 al., 2009), extinction less than 0.5 km^{-1} (Febvre et al., 2009), and IWC up to 10 mg m^{-3} (Schröder et
131 al., 2000; De Leon et al., 2012). At this stage, within a sustained ice-supersaturated environment,
132 contrail microphysical properties may still differ from those of natural cirrus (Voigt et al., 2017) with
133 concentrations of ice crystals larger than $100 \mu\text{m}$ in the order of 0.1 cm^{-3} . These crystals typically
134 show bullet rosette type habits (Heymsfield et al., 1998; Heymsfield et al., 2010). Optical depth values
135 can reach values of 2.3 (Atlas and Wang, 2010), corresponding to an extinction of 0.023 km^{-1} .

136 Nevertheless, the transition from contrails to cirrus highly depends on the ambient saturation
137 conditions. Modelling studies with typical atmospheric conditions show a temporal evolution of the
138 optical and microphysical properties when contrails evolve to contrail cirrus clouds (Burkhardt and
139 Kärcher, 2011; Unterstrasser et al., 2016 ; Schumann et al., 2015).

140 In this study, we report on a powerful alternative to classify cloud events into young contrail
141 and contrail-cirrus. The method is applied to aircraft data of the CONCERT (Contrail and Cirrus
142 Experiment) campaigns (Voigt et al., 2010, 2011, 2014). The methodology consists in implementing
143 a Principal Component Analysis (PCA) of the angular light scattering data measured by the Polar
144 Nephelometer. The PCA patterns are classified to yield different cluster representing specific contrail
145 types. Corresponding optical, microphysical, and chemical properties are derived for each contrail
146 phase (from young contrails to cirrus contrails). This paper starts with an overview of the properties
147 of contrails and cirrus clouds observed during two specific CONCERT flights (19 November 2008
148 and 16 September 2011) encompassing a series of different contrail evolution stages. These two
149 flights containing a variety of contrail-cirrus information can be regarded as an analytical framework
150 producing results which then can be compared to contrail-cirrus properties of other flights.

151 **2 CONCERT projects and data processing**

152 2.1 CONCERT campaigns

153 CONCERT-1 and CONCERT-2 campaigns took place in October/November 2008 and
154 August/September 2011, respectively. These two campaigns with the DLR Falcon 20 E research
155 aircraft were based in Oberpfaffenhofen, Germany, and sampled contrails and cirrus at mid-latitudes
156 over Europe. The overall objective was to reduce uncertainties on the microphysical, chemical, and
157 radiative properties of contrails behind aircraft of different types and to improve the evaluation of
158 contrail's impact on climate. A few CONCERT flights were also dedicated to study emissions of Etna
159 and Stromboli volcanos (Voigt et al., 2014; Shcherbakov et al., 2016). A few stratospheric intrusions
160 were also observed during the flight missions. In total, 23 flights were recorded during the two
161 measurement campaigns, wherein 12 flights were entirely focused on aircraft contrail chasing.
162 Overall, more than 17 different aircraft exhausts plumes have been probed. CONCERT-2 campaign
163 mainly focused on the observation of persistent contrails, and hence on the evolution of contrails to
164 contrail cirrus.

165 During both CONCERT campaigns, the DLR research aircraft Falcon was equipped with a
166 set of instruments to measure the optical and microphysical properties of cloud particles and also the
167 trace gas composition in the UTLS (Upper Troposphere / Lower Stratosphere) region. Voigt et al.
168 (2010) provide a detailed description of the aircraft instrumentation. We briefly introduce the
169 instruments used in this study.

170 2.2 Aircraft instrumentation

171 The microphysical and optical particle properties of contrails and cirrus presented in this study
172 were mainly derived from the PMS Forward Scattering Spectrometer Probe 300 (FSSP-300), the
173 Polar Nephelometer (PN), and the PMS 2D-C hydrometeor imaging probe. The combination of these
174 independent techniques characterizes cloud particles within a range of diameters varying from 0.5
175 μm to 2 mm.

176 The PN (Gayet et al., 1997) measures the angular scattering coefficients (non-normalized
177 scattering phase function) of an ensemble of water droplets or ice crystals or a mixture of those
178 particles ranging from a few micrometers to approximately 1 mm in diameter. These particles

179 intersect a collimated laser beam, at a wavelength of 804 nm, near the focal point of a parabolic
180 mirror. The light scattered at angles from 3.49° to 172.5° is reflected onto a circular array of 56 near-
181 uniformly positioned photodiodes. In this study, reliable measurements were performed at 30
182 scattering angles ranging from ±15° to ±162°. Particle phase (water droplets and/or ice crystals) can
183 be assessed as well as single scattering properties such as the extinction coefficient and the asymmetry
184 coefficient with uncertainties of 25% and 4%, respectively (Gayet et al., 2002; Jourdan et al., 2010).

185 Particle size distributions and corresponding microphysical and optical integrated properties
186 (IWC, Deff, N, and extinction) were derived from both FSSP-300 and 2DC measurements. The FSSP-
187 300 (Baumgardner et al., 1992) measures the intensity of forward scattered light from cloud particles
188 passing through the laser beam, with cloud particles in the diameter range 0.35-20 µm. In the forward
189 angular region (from 4° to 12°), scattering is mainly described by the particle diffraction pattern and
190 therefore depends on the refractive index, the shape, and the size of the particles. The method of data
191 processing and size calibration used during the CONCERT campaigns have been presented in Gayet
192 et al. (2012). We briefly recall that the asymmetry parameter derived from the PN was used to
193 discriminate nearly spherical particles ($g \geq 0.85$) from non-spherical ones ($g < 0.85$) at 804 nm. For
194 spherical ice particles, Mie calculations were used to derive the size bin limits and the corresponding
195 extinction efficiency. Results were adjusted to the calibrated probe response. Additionally, to
196 minimize Mie ambiguities related to the FSSP-300 size response, 31 channels were rebinned to 13
197 channels with a diameter ranging from 0.5 µm to 18 µm (upper channels 30 and 31 were excluded
198 from the data analysis). For non-spherical particles, the size of the contrail particles is expressed in
199 terms of an equivalent surface or area diameter, i.e. the diameter of a sphere that has the same area
200 than the projected area of the measured non-spherical particle image (Mishchenko et al., 1997;
201 Schumann et al., 2011). The particles were assumed to be rotationally symmetric ice ellipsoids with
202 an aspect ratio of 0.5. Accordingly, and contrary to the method used for spherical particles, 15 size
203 bins ranging from 0.5 µm to 18 µm were defined based on T-Matrix calculations following Borrmann
204 et al., (2000).

205 The bi-dimensional optical array spectrometer probe (2DC) provides information on the
206 crystal size and shape within a nominal size range from 25 µm to 800 µm by recording cloud particles
207 shadow images with a 25 µm resolution. The method of data processing used in this study is described
208 in detail in Gayet et al. (2002) and Febvre et al. (2009). Reconstruction of truncated particles has been
209 considered for the PSD calculations and the sampling surfaces have been derived according to
210 Heymsfield and Parrish (1978). To improve the statistical significance of low particle concentrations,
211 a 5-s running mean was applied. As the sensitivity of the probe to small particles decreases with
212 airspeed (Lawson et al., 2006), particles smaller than 100 µm may not be detectable at the Falcon
213 airspeed of typically 180 m s⁻¹. This may result in larger uncertainties of up to 100% in the derived
214 microphysical parameters such as the IWC (Gayet et al., 2002 and 2004).

215 For spherical and non-spherical particles, the extinction coefficients are calculated from the
216 following equation:

$$Ext = \frac{\pi}{4} \sum_i \beta_{ext}^i N_i D_i^2 \quad (1)$$

217 where β_{ext}^i is the extinction efficiency (values depend on spherical or aspherical particle
218 characterization), D_i the mean diameter in channel i , and N_i the number concentration.

219 Different approaches are used to retrieve ice water content from spherical and non-spherical
220 particles (Garret et al., 2003 ; Gayet et al., 2004 ; Gayet et al., 2012). For spherical particles ($g_{PN} >$
221 0.85), IWC is computed from the following equation:

$$IWC_{spherical} = \frac{\pi}{6} \rho_{ice} \sum_i N_i D_i^3 \quad (2)$$

222 with ρ_{ice} the bulk ice density (0.917 g cm^{-3}).

223 For non-spherical ice crystals ($gPN < 0.85$ and for particle diameters larger than $50 \text{ }\mu\text{m}$), an
 224 equivalent diameter method is used (Gayet et al., 2004). For an ice crystal with an area A , the particle
 225 equivalent diameter D_{equ} (in mm for eq. (3) and (4)), the equivalent mass x_{equ} (in mg), and the Ice
 226 Water Content (IWC in mg m^{-3}) are defined as:

$$A \leq 0.049 \text{ mm}^2 \quad D_{equ} = 0.82A^{0.48} \quad (3)$$

$$A > 0.049 \text{ mm}^2 \quad D_{equ} = 0.56A^{0.32} \quad (4)$$

$$x_{equ} = \frac{\pi}{6} \rho_{water} D_{equ}^3 \quad (5)$$

$$IWC_{non-spherical} = \sum_i N_i x_{equ} \quad (6)$$

228 with ρ_{water} the bulk water density (1 g cm^{-3}).

229 These equations do not account for possible shattering of large ice crystals on the probe inlets.
 230 This effect is minor in young contrails but can lead to an underestimation of large ice crystal
 231 concentration (diameters higher than $100 \text{ }\mu\text{m}$) and thus an overestimation of small ice crystal
 232 concentration in contrail cirrus clouds (Febvre et al., 2009).

233 Trace gas measurements were also performed. NO/NO_y concentrations can be significant in
 234 young tropospheric aircraft plumes. NO and NO_y mixing ratio were performed using the
 235 chemiluminescence technique (Schlager et al., 1997) with a time resolution of 1 s. Instruments used
 236 for CONCERT campaigns are described in several studies (Jurkat et al., 2010 ; Jurkat et al., 2011 ;
 237 Voigt et al., 2014 ; Jurkat et al., 2016). The accuracy (and precision) of the NO and NO_y
 238 measurements are estimated with 7% (and 10%) and 10% (and 15%), respectively (Ziereis et al.,
 239 2000).

240 Relative humidity with respect to ice (RHI) is also key parameter to understand contrail
 241 formation and microphysical properties. Water vapour was measured with the chemical ionization
 242 mass spectrometer AIMS-H₂O during CONCERT-2 (Kaufmann et al., 2014; 2016). Hygrometers
 243 using the Lyman- α technique (FISH, Zöger et al., 1999; Meyer et al., 2015), and frost point
 244 hygrometers (CR-2, Heller et al., 2017) were deployed on the Falcon during CONCERT-1 and 2.

245 3 Results

246 3.1 Overview of the cloud properties sampled during the reference cases

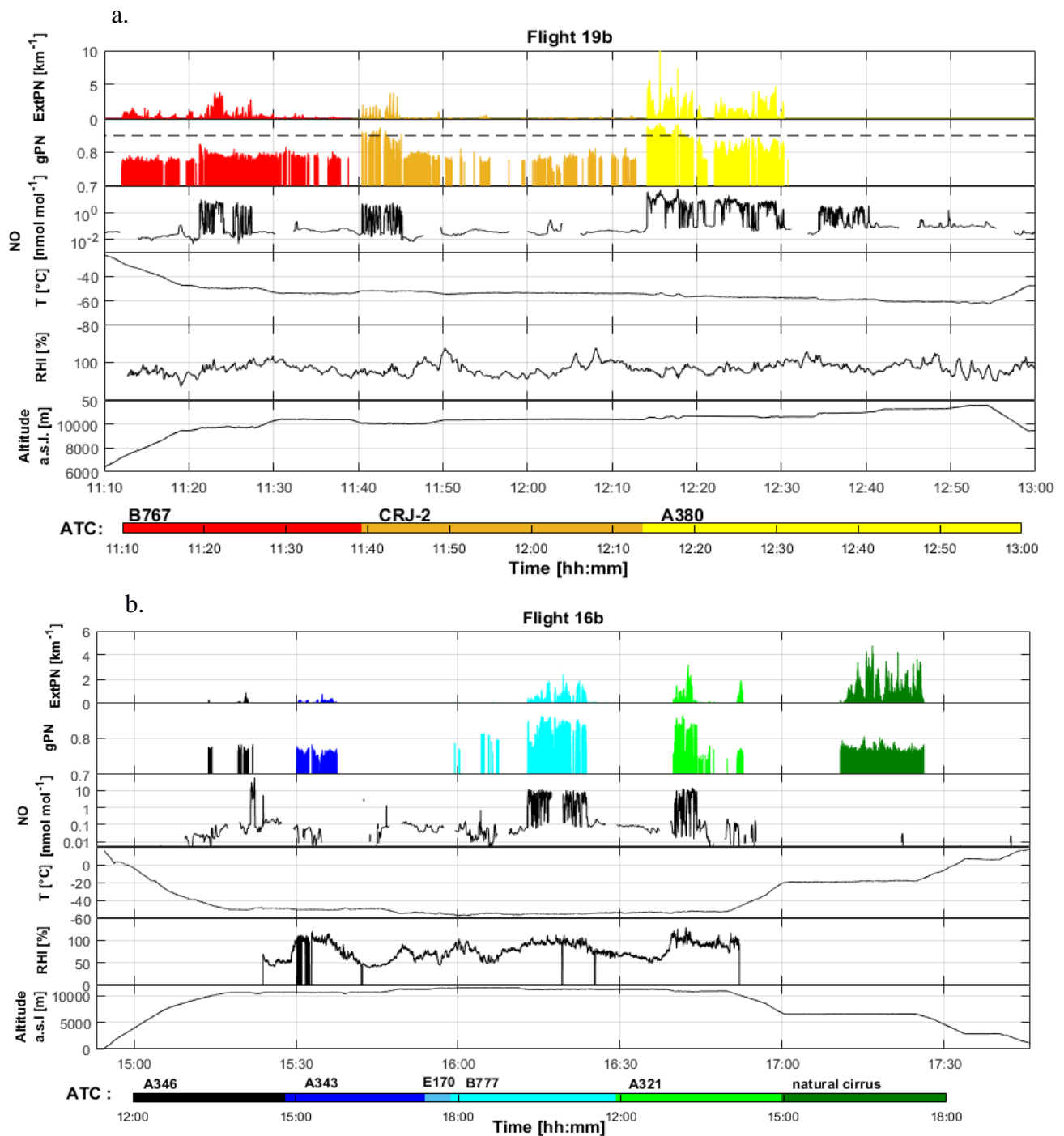


Figure 1: Time series at 1 s resolution for flights a) 19b (CONCERT 1) and b) 16b (CONCERT 2). From top to bottom: extinction coefficient (in km^{-1}) and asymmetry parameter measured by the Polar nephelometer at 804 nm (dashed line corresponds to a 0.85 value), concentration of nitric oxide (in nmol mol^{-1}) measured by chemiluminescence technique, temperature (in $^{\circ}\text{C}$), relative humidity with respect to ice (in %), and altitude a.s.l. (in m). Temporal series are coloured according to time and aircraft chasing information from Air Traffic Control (ATC).

247 The purpose of this section is to give an overview of the contrail optical properties and more
 248 interestingly to evaluate the ability of the Polar Nephelometer measurements to identify contrails.
 249 Two flights, performed on 16 September 2011 during CONCERT-2 (flight 16b) and on 19 November
 250 2008 during CONCERT-1 (flight 19b), respectively, were selected for their variety of contrails and
 251 cirrus sampled during these two flights. The two flights are considered as a benchmark to illustrate
 252 the potential of the PCA methodology described in Sect. 3.2.

253 Figure 1 displays the time series of the extinction coefficient (ExtPN) and the asymmetry
254 parameter (gPN) at a wavelength of 804 nm, relative humidity with respect to ice (RHI), the nitric
255 oxide (NO) concentration, the temperature T and the altitude for flights 19b and 16b. RHI measured
256 with the AIMS mass spectrometer is shown for flight 16b. RHI measurements during flight 19b as
257 well as instrument shortcomings are discussed in details in Kübbeler et al. (2011), Gayet et al. (2012),
258 Jessberger et al. (2013) and Schumann et al. (2013). For both flights, Air Traffic Control (ATC)
259 provides information on the flight tracks and on the chased aircraft (aircraft type, engine type, fuel
260 flow, weight, engine power setting). From this information the Falcon measurements were attributed
261 to the exhaust plume of individual aircraft with an estimated plume age. Time series are colour coded
262 according to ATC information.

263 The PN extinction coefficient coupled with the asymmetry parameter seems to be a reasonable
264 proxy to detect contrails and cirrus clouds (see amongst other references, Voigt et al., 2010). ExtPN
265 values, by definition, depend on the cloud particle concentration and size. Values typically beyond
266 0.1 km^{-1} correspond to cloud events that are well correlated to environmental conditions
267 supersaturated with respect to ice ($\text{RHI} > 100\%$). Figure 1 shows that relatively high values of
268 extinction can be found in flights 19b and 16b that are linked to the presence of contrails or cirrus
269 clouds. Moreover, the temporal distributions of these values are in accordance with ATC information
270 for both flights. For instance, most of the contrails induced by commercial aircraft exhaust plumes
271 are associated with significant extinction coefficient values. The ExtPN values are between 0.2 km^{-1}
272 and 10 km^{-1} for contrails induced by A346, A340, and A380 commercial aircraft. Cirrus clouds are
273 detected with more variable extinction values mostly larger than 0.5 km^{-1} . Most of the aircraft induced
274 contrails are detected by the PN except for the ones stemming from the E170 airplane. At 15:50 during
275 flight 16b, ATC identified the E170 position close to the Falcon flight trajectory, however the ExtPN
276 and the NO mixing ratio remained very low. Hence, the E170 contrail was not probed by the Falcon.
277 In the following we assume that only periods with ExtPN values above 0.1 km^{-1} are considered as a
278 reliable signature of contrails.

279 The absolute values of the asymmetry parameter gPN provide additional information on the
280 cloud particle shape. Indeed, gPN is a good indicator of the degree of sphericity of ice crystals (Gayet
281 et al., 2012). Ice clouds with gPN values higher or equal to 0.85 are typically composed of spherical
282 ice crystals, whereas lower values are indicative of aspherical ice particles. In a supersaturated
283 environment, crystals grow by water vapour deposition and become increasingly aspherical with time.
284 However, in very young contrails, spherical ice crystals with an asymmetry coefficient around 0.85
285 prevail. gPN is decreasing when water vapour diffusion is generating more and more aspherical
286 crystal shapes at ice supersaturation. This can be observed for A321 chasing during flight 16b where
287 gPN is decreasing to a value of 0.75 whilst RHI remains around 100%. This is not the case during
288 B777 chasing where no gPN decrease is observed when $\text{RHI} < 100\%$. However, it is important to
289 note that the RHI measurements during the CRJ-2 chasing events do not show supersaturated
290 conditions, whereas contrail seems persistent. Indeed, RHI measurements should be discussed
291 carefully for this campaign due to calibration issues.

292 Natural cirrus clouds are mainly composed of non-spherical ice crystals. These clouds can be
293 easily discriminated from young contrails as they exhibit a much lower asymmetry parameter
294 typically below 0.75 (see amongst others Jourdan et al., 2003b, Febvre et al., 2009). However, no
295 accurate ambient RHI data can be retrieved for measurements in “natural” cirrus due to instrumental
296 calibration problems. A good example of the evolution of gPN is the CRJ-2 contrail observed between
297 11:40 and 11:45 during flight 19b. The sequence illustrates the potential of the gPN measurement to
298 characterize the evolution of contrail properties. The evolution of the ice crystal shape is reflected in
299 the decrease of the asymmetry parameter from 0.88 to 0.79 (uncertainties around 0.04) after only 5
300 min and down to 0.77 after 20 min. A weaker decrease of gPN values (around 0.78 ± 0.02) is then

301 observed until 12:10 corresponding to 30 min of contrail ageing. During this period, ice crystals are
302 expected to grow by water vapour diffusion. A similar decrease of gPN values has been reported by
303 Gayet et al. (2012) in the ageing contrail from an A380 aircraft, and is also visible in the present study
304 for the B767 and the A321 contrails.

305 NO concentration measurements can also be used to discriminate natural cirrus clouds from
306 ice clouds influenced by aircraft traffic. At the typical altitude of 10 km, NO environmental
307 concentrations are close to background values. In contrast, NO concentrations in young contrails may
308 reach several tens of nmol mol^{-1} (Voigt et al., 2010). Figure 1 shows a good correlation between the
309 expected localization of young contrails and NO concentrations. The dilution effect in the upper
310 troposphere causes an important decay of chemical concentrations. For instance, the first few seconds
311 of the A380 chasing during flight 19b are characterized by a high NO concentration (up to 40 nmol mol^{-1})
312 followed by a fast decrease to 10 nmol mol^{-1} in the next 15 min, and less than 5 nmol mol^{-1}
313 beyond 15 min. NO concentrations finally decrease to background levels within hours (e.g. Voigt et
314 al., 2017). This decrease of the NO concentration is in accordance with the decrease of the extinction
315 coefficient (from 10 to 0.2 km^{-1}) and asymmetry parameter (from 0.88 to 0.77). NO is mainly used
316 as an additional contrail indicator. However, during some aircraft chasing events, NO concentrations
317 were near background levels, while mass spectrometric measurements (not shown here) indicate
318 elevated concentrations of HONO, HNO_3 , and SO_2 representative for contrail chemical species.

319 Flights 19b and 16b clearly show that the optical properties of contrail clouds (supported by
320 the ATC information) in conjunction with specific trace gas concentration measurements can be used
321 to discriminate contrails from natural ice cloud events. A first order analysis of these parameters can
322 be used to roughly distinguish young contrails (mostly quasi-spherical ice crystals) from aged
323 contrails (mostly aspherical ice crystals) and natural cirrus (background NO concentrations). This
324 analysis is mainly qualitative and based solely on a few typical parameters (Fig. 1). A more robust
325 statistical method should be used to accurately separate the different contrail phases. In the following
326 section, relationships between contrail and ice cloud properties scattering properties are investigated
327 more extensively to assess whether the information content of the PN scattering measurements is
328 sufficient to document changes in the contrail microphysical properties.

329 **3.2 Statistical Method**

330 In this section, we present a methodology based on the statistical analysis of the optical
331 signature of contrails and cirrus. The goal is to classify the contrail properties according to the
332 aircraft origin and evolution stage. The main objective of the Principal Component Analysis (PCA)
333 is data reduction to allow a better physical interpretation of the light scattering patterns derived from
334 the Polar Nephelometer measurements (Legendre and Legendre, 1998; Jourdan et al., 2003). In this
335 study, optical properties of ice crystals in the evolving contrail environment are examined to evaluate
336 contrail evolution. This statistical analysis was already successfully applied to discriminate mixed
337 phase clouds (Jourdan et al., 2003 ; Jourdan et al., 2010) from liquid clouds and ice clouds, and to
338 identify porous aerosol in degassing plumes (Shcherbakov et al., 2016).

339 **3.2.1 Reference definition**

340 The PCA is first applied to the PN angular scattering coefficients measurements performed
341 during flights 16b and 19b which are here considered as our reference dataset. Initially, a correlation
342 matrix is calculated to characterize the link between each scattering angle. The PCA is designed to
343 generate a new limited set of uncorrelated parameters, called principal components C_{lj} representative
344 of the original data set variability.

345 A first implementation of the PCA is performed to detect unreliable data or out of order
 346 photodiodes. For instance, seven photodiodes presented a low signal to noise ratio and were excluded
 347 from the dataset. Flight sequences characterized by $\text{ExtPN} < 0.1$ were also removed. Finally, flight
 348 sequences dedicated to aircraft chasing and ice cloud sampling were considered to perform a second
 349 PCA. The analysis is performed on the remaining angular scattering coefficients (4669 Angular
 350 Scattering Coefficients (ASC) representing PN measurements of flights 16b and 19b) restricted to 25
 351 angles θ ranging from 15° to 155° . The new set of variables or coordinates, C_{ij} , can be expressed
 352 with the scalar product of the vector of reduced angular scattering coefficients $\overrightarrow{\sigma}_j(\theta)$ for the j^{th}
 353 measurements, expressed in log scale, and the l^{th} eigenvector $\xi_l(\theta)$ (i.e. principal component) of the
 354 total data set correlation matrix (Jourdan et al., 2010).

$$C_{ij} = (\overrightarrow{\ln\sigma_j} - \langle \overrightarrow{\ln\sigma} \rangle)^T \cdot \overrightarrow{\xi_l} \quad (4)$$

355 where $\langle \overrightarrow{\ln\sigma} \rangle$ represents the average ASC of the dataset.

356 The first three eigenvectors $\overrightarrow{\xi_l(\theta)}$ of the correlation matrix are displayed in Fig. 2 along with
 357 their normalized eigenvalues λ_l , representing more than 99% of the variability of the PN angular
 358 scattering coefficients (ASC).

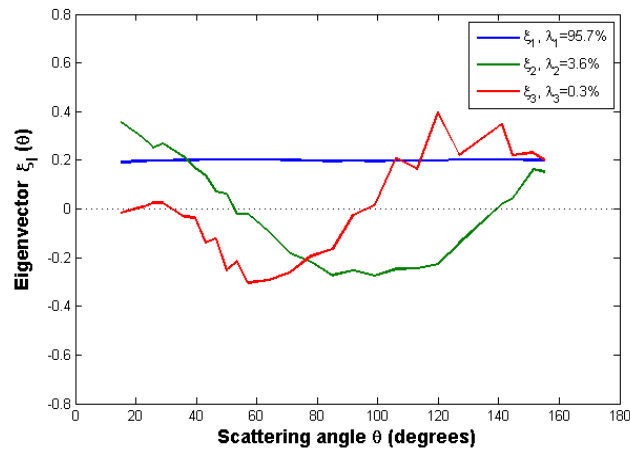


Figure 2: First three eigenvectors for the flights 16b and 19b.

359 The first eigenvector $\xi_1(\theta)$ is approximately constant versus scattering angle and represents
 360 95.7% of the total variance. It means that this principal component is representative of changes of the
 361 magnitude of phase functions without any changes in their global shape. This behaviour means that
 362 95.7% of the ASC variations are linked to changes of the cloud particle extinction. Results show a
 363 good correlation ($r^2 = 0.98$) between the first eigenvector and the extinction derived from the PN
 364 measurements (ExtPN).

365 The second eigenvector $\xi_2(\theta)$ reverses sign twice at scattering angles equal to 50° and 140°
 366 with an extremum around 90° . Accordingly, 3.6% of the angular scattering variability corresponds to
 367 a redistribution of scattered energy from the angular region (50° - 140°) to scattering angles lower than
 368 50° and higher than 140° . Light-scattering modelling studies demonstrate that the scattering
 369 behaviour in the angular region between 60° and 140° is sensitive to the particle shape and
 370 thermodynamic phase (Jourdan et al., 2010). A strong linear correlation ($r^2=0.97$) between the second
 371 eigenvector and the asymmetry coefficient (gPN) at 804 nm is found.

372 The third eigenvector represents only 0.3% of the total variance. However, this eigenvector
 373 provides additional information in scattering regions which are not well described by the first two
 374 principal components. It has opposite signs in the angular region (30°-90°) and (90°-155°) with
 375 maximum extremal values at 60° and 120°. The shape of the third eigenvector describes the
 376 forward/backward hemisphere partitioning of the scattering. Baran et al. (2012), Xie et al. (2006),
 377 and Xie et al. (2009) showed that the scatter pattern for angles between 120° and 160°, corresponding
 378 to ice bow-like effects, is sensitive to quasi-spherical particles. Moreover, these backscattering angles
 379 ($\theta > 120^\circ$) and scattering angles around 22° and 46° (corresponding to halo features) can also be linked
 380 to the particle habits and surface roughness (Xie et al., 2009, Jourdan et al., 2010).

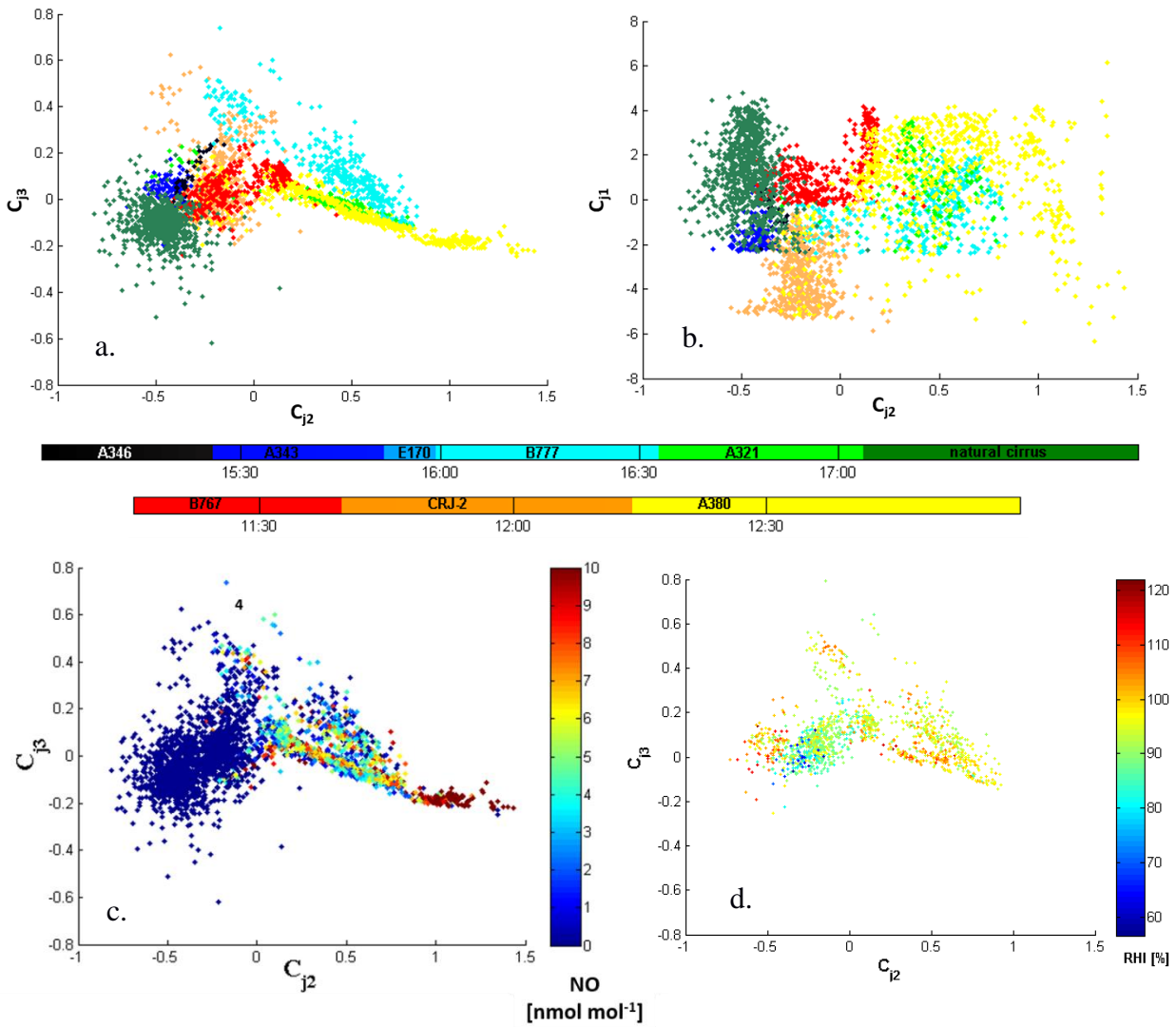


Figure 3: Expansion coefficient diagram for flights 16b and 19b: third versus second principal component for a), c) and d), and first versus second principal component for b). Data points are colour coded according to ATC information for a) and b), by NO concentration for c), and by RHI values for d).

381 Each phase function (or ASC) measured by the PN can be expressed with a good accuracy as
 382 a linear combination of the three principal components (Jourdan et al., 2010). The PN data are
 383 projected into a new space defined by the three principal components (3D-space) instead of the 25-
 384 dimensional space of ASC. The scatterplots of the C_{j3} and C_{j1} expansion coefficients versus the C_{j2}
 385 coefficient are represented on Fig. 3a and b respectively. Fig. 3a illustrates the features of the ASC
 386 measurements in one of the most comprehensive way. Each point corresponds to a measured phase
 387 function documented over 25 angles. The variability of C_{j2} coefficients is significant with values

388 ranging from -1 to 1.5. The angular variation of the second principal component indicates that large
389 values of C_{j2} ($C_{j2} > 0.75$) correspond to ASC with low side scattering (60° - 130°) and higher forward
390 scattering (15° - 40°) and somehow higher backscattering (145° - 155°). This behaviour is connected to
391 an increase of the asymmetry parameter with an increase of C_{j2} values. Thus, the fraction of spherical
392 particles increases with increasing C_{j2} . In the region defined by negative values of C_{j2} the density of
393 points is relatively high. These cloud events exhibit optical properties characterized by a large side
394 scattering and low asymmetry parameter. Therefore, specific cloud sequences sharing similar
395 scattering properties can be identified based on this second principal component. Young contrails
396 characterized by quasi-spherical ice crystals have high positive values of C_{j2} while cirrus clouds and
397 contrail cirrus exhibit high negative values.

398 In the space of the third principal component high positive values of C_{j3} imply that less energy
399 is scattering in the forward hemisphere and thus more energy is scattered in the backward hemisphere.
400 The variability of the expansion coefficients is less pronounced as ASC are distributed between -0.4
401 and 0.6. Most of the measured ASC do not significantly differ from the average ASC in the angular
402 ranges (30° - 90°) and (90° - 155°). However, some specific clusters linked to scattering behaviour can
403 be identified for values of C_{j3} greater than 0.1 and lower than -0.1. These threshold values also depend
404 of the position of the ASC on the second principal component. Finally, the first principal component
405 is directly linked to the extinction coefficient. High values of C_{j1} are representative of optically dense
406 cloud sequences.

407 Figure 3c shows an increase of C_{j2} for increasing NO mixing ratio. This clearly indicates that
408 the contrails are evolving in space and/or time along the Falcon flight track. Cloud regions influenced
409 by air traffic can be discriminated from clouds formed by natural processes based on the NO
410 concentration values. Hence, contrails characterized by a low side scattering due to the presence of
411 spherical ice crystals correspond to high NO concentration. This behaviour can be a signature of
412 young contrail properties. Elder or aged contrails composed of a higher fraction of non-spherical
413 crystals or growing more aspherically are expected to exhibit an enhanced side scattering and a lower
414 asymmetry parameter associated to lower NO concentrations. RHI measurements also give relevant
415 information on the capacity of the cloud to be persistent. Thus, Fig. 3d shows higher RHI values with
416 decreasing gPN values.

417 **3.2.2 Clustering analyses**

418 The new representation of each measurement in the space of the first three principal
419 component reveals different clusters, characteristic of specific scattering behaviour. The clustering k-
420 mean method (Seber 1984, Spath 1985) is applied to the reference dataset (flights 19b and 16b) to
421 partition the observations into k clusters to minimize the variance within each cluster (i.e. to minimize
422 the distance between each data point and the centre of the cluster it belongs to). The number of cluster
423 k is an adjustable parameter. Then in a first step, each observation is assigned to a specific cluster
424 whose mean has the least squared Euclidean distance (i.e. nearest mean). In a second step, the position
425 of each cluster is set to the mean of all data points belonging to that cluster (i.e. the centroids of each
426 of the k clusters becomes the new means). These two steps are repeated until convergence is reached
427 when the assignments no longer change.

428 16 clusters were found to encompass all points of the two flights and to partition each aircraft
429 chasings identified from ATC information (Fig. 3a and 3b). For clarity and better understanding of
430 the variability of contrail properties, we choose to limit the number of clusters to 6. 9 clusters are
431 merged into 2 clusters to define the group “cirrus” and B767 / A343 / CRJ-2 contrails (referred
432 hereafter to Cluster 3 and 5 respectively). 4 clusters are also gathered in one new cluster
433 corresponding to A321 / A380 contrails (referred to Cluster 2 hereafter). In addition, only data within

434 the 10% of the maximum Mahalanobis distance (De Maesschalck et al., 2000) to the respective
 435 cluster's centre has been considered for this analysis.

436 Clusters are defined by their means (or centres), standard deviations (or widths), and cross-
 437 correlations (or tilts). The Mahalanobis distance is given by the equation:

$$D_M(x)_i = \sqrt{(x - \mu_i)^T S_i^{-1} (x - \mu_i)} \quad (5)$$

438 with D_M the Mahalanobis distance between point x and the i^{th} cluster center, μ_i the N-dimensional
 439 mean of this cluster and S_i its covariance matrix.

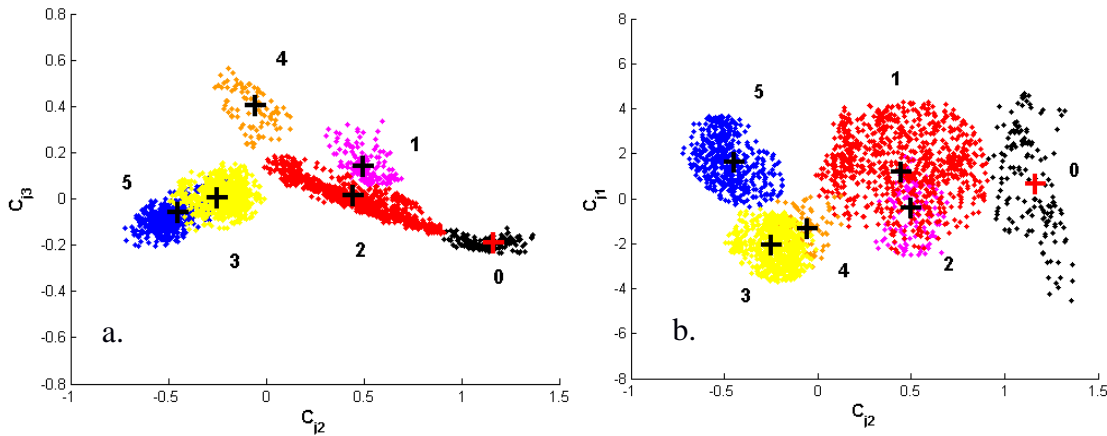


Figure 4: Clustering results of the k-mean method applied to the base (flights 16b and 19b). Third versus second principal component for a), and first versus second principal component for b). Only data within the 10% of the maximum Mahalanobis distance to the respective cluster's centers have been considered for this analyse.

440 Figure 4 shows the partitioning of the dataset into the 6 new clusters (clusters 0 to 5). In the
 441 following we use data from chemical tracers and optical measurements, and aircraft type information
 442 to support and discuss the results of the k-means clustering method.

443 While clusters 3 and 5 are characterized by very low NO concentrations (close to zero, Fig.
 444 3c) above background, clusters 0, 1, 2, and 4 correspond to higher concentrations representative of a
 445 significant aircraft exhaust influence. ATC information shows that cirrus clouds are gathered in
 446 cluster 5. Most of the contrails induced by the B767, A343, A346 and CRJ2 aircraft are associated to
 447 cluster 3 or 5. These cloud events share similar optical properties characterized by a low asymmetry
 448 parameter, high side scattering behaviour, and supersaturated ambient conditions with respect to ice
 449 for some cases. Contrails relative to the A380 aircraft are dispatched in cluster 0 and 2 while the ones
 450 corresponding to the B777 are spread out between clusters 1 and 4.

451 The contrail and cirrus classification based on ASC measurements appears to be consistent
 452 with the independent trace gas measurements. Each cluster represented on Fig. 4 can be linked to a
 453 distinct cloud event. Therefore, the combination of flights 16b and 19b can provide a relevant test-
 454 bed database to discriminate contrail properties. Young contrails (spherical ice crystals) are associated
 455 to clusters 0, 1 or 2, whereas aged contrails (aspherical ice crystals and high RHI values) with more
 456 pristine ice are categorized in clusters 3 and 4, and finally cirrus (low NO concentrations) are found
 457 in cluster 5. A less precise analysis (using onboard camera) reveals that cluster 0 corresponds
 458 essentially to the primary wake created below the secondary wake behind an aircraft. Table 1
 459 summarizes these cluster's definitions and names used in this work.

Cluster number	definition	name
0	Primary Wake	PW
1	Young Contrail 1	YC1
2	Young Contrail 2	YC2
3	Aged Contrail 1	AC1
4	Aged Contrail 2	AC2
5	Cirrus Cloud	CC

Table 1: Cluster's definitions according to ATC information and tracer measurements (NO concentrations and RHI values)

461 One should keep in mind that some points are still arbitrarily attributed to a particular cluster
462 without strong physical justification.

463 3.2.3 Merging other CONCERT flights

464 In this section we complement the previous analysis with additional cloud optical
465 measurements performed during other CONCERT flights to increase the robustness of the method.

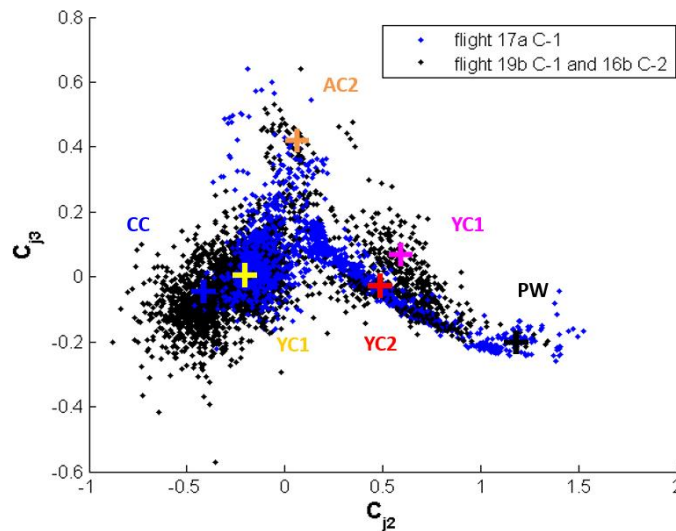


Figure 5: Example of data projection in the C_{j2}/C_{j3} space where data from flight 17a (blue data points) are superposed on the data from the benchmark flights 19b and 16b (black data points).

466 The ASC measured during other flights can be projected in the space of the principal
467 components established with flights 16b and 19b dataset. The coordinates of the data points
468 corresponding to the other flights are calculated from Eq. (4). An example of this data projection
469 is illustrated in Fig. 5 where flight 17a is represented in the C_{j2}/C_{j3} space. Each data point
470 can be attributed to one cluster previously defined by the k-mean clustering method based on
471 flights 16b and 19b dataset (black points). In other words, the ASC measured during another
472 flight can be merged (projected) into the expansion coefficient diagram displayed on Fig. 3.
473 Data points sharing similar optical properties will be close to each other on such plot. Figure
474 5 shows that different contrail phases are observed during flight 17a. Data points are mostly
475 grouped into cluster AC1, but are also present in clusters AC2, YC2, and PW. Finally, cloud
476 data gathered during this flight are mainly categorized as young and aged contrails. We follow
this methodology to project and classify each additional

477 “contrail” event performed during both CONCERT campaigns with minimum Mahalanobis distance
 478 (see Eq. (5)).

Day / Aircraft		Cluster	Cluster				Number of points	Age (s)		
			PW	YC1	YC2	AC1			AC2	CC
			1st wake	young contrails	aged contrails	Cirrus				
17a C-1	TOTAL						1435			
	A340-311						359	61 - 144		
	TOTAL						2715			
	B737-500						310	77 - 151		
	A340-642						100	82 - 139		
	NC						189	-		
	TOTAL						2152			
	A319-111						628	94 - 129		
	A340-311						175	63 - 90		
	TOTAL						1647			
B767-300						319	77 - 107			
CRJ-2						151	80 - 95			
A380-841						677	109 - 240			
TOTAL						1434				
B737-300						64	90 - 290			
TOTAL						1511				
A340-600						128	100 - 132			
B777						378	120 - 160			
A321						135	70 - 95			
TOTAL						2904				
NC1						498	-			
NC2						233	-			
TOTAL						1380				
B777						371	112 - 178			

Table 2: Classification relative to the six clusters on the Cj2/Cj3 representation of the PCA of all data points for each flight of the two CONCERT campaigns (C-1 in November 2008 and C-2 in September 2011). The legend of the bars represents the relative contribution of data points of individual contrails (blue bars) and also entire flights (black bars) to the 6 individual clusters.

479 The assignment of the data points to the six clusters shown on the expansion diagrams is
 480 summarized in Table 2. 8 flights (6 additional flights) representing 4426 ASC measurements were
 481 processed. The lengths of the bars in Table 2 represent the distribution of the data points within the
 482 different clusters: a) black bars correspond to the fraction of cloud events within a specific flight (with
 483 extinction coefficient higher than 0.1 km^{-1}) and b) blue bars represent cases of individual contrails
 484 within the flight. Data points with extinction coefficient lower than 0.1 km^{-1} are not shown in the
 485 table. More than 30% of the data points are located in clusters AC1 and/or CC meaning that they
 486 correspond to aged contrail and sometimes cirrus. Flights clearly performed in well visible contrails
 487 outside cirrus (earlier development stage and/or intensified persistent elder contrails) exhibit
 488 significant fraction of data points associated to clusters PW, YC1, and YC2 (young contrails) for both
 489 CONCERT-1 and CONCERT-2 campaigns. However, within these flights data points are also
 490 gathered in cluster AC1 (aged contrails clean) and to a lesser extent in cluster AC2 (aged contrails,
 491 mostly corresponding to measurements performed during two different B777 contrail chasing events).

492 These results are in reasonable agreement with previous conclusions (this subsection) drawn
 493 for the cluster definitions and associated contrail / ice cloud characteristics. Very young contrails have
 494 been mostly chased during CONCERT-1 (flights 19a and 19b). Another interesting result is related
 495 to flight 17 during CONCERT-2 (flight 17 C-2) where no aircraft information was provided by ATC.
 496 Still ATC data indicate measurements in exhaust plumes and the Falcon flew apparently in visible
 497 contrails ($\text{ExtPN} > 0.1 \text{ km}^{-1}$) which were probably too old for ATC recognition. Our analysis shows

498 that these data points can mainly be attributed to cluster CC and AC1. This observation suggests that
499 significantly aged contrails have been sampled. However, crystal formation and growth processes in
500 contrails and natural cirrus suggest that very old contrails more and more resemble natural cirrus
501 properties.

502 ATC information on exhaust plume ages was also collected during each chasing. Some
503 chasings were performed less than 100 s after contrail formation. This is the case for the A340 contrail
504 during flight 19a and for the CRJ-2 contrail during flight 19b of CONCERT-1 and for the A321
505 contrail during flight 16b of CONCERT-2. One can notice that the contrail ages are well correlated
506 to the chosen cluster definitions, revealing that contrail data relative to the A340 are included in
507 cluster PW and YC2 (young contrails) for more than 90% of the data points, and nearly 63% for the
508 CRJ-2 and 84% for the A321. According to our cluster classification, only 5% of the data points
509 gathered during these three flights correspond to aged contrail (cluster AC1 and AC2) categories in
510 contrast to other CONCERT-1 and CONCERT-2 flights (with more than 30% of data points
511 associated to AC1 and AC2). Even though it is still difficult to associate contrail ages to measurement
512 points, the “contrail age” ranges agree with the cluster definitions.

513 **4 Evolution of contrail properties**

514 **4.1 Optical and chemical cluster properties**

515 In the previous section we showed that cloud events can be separated according to their light-
516 scattering properties. Six clusters were defined based on two flights having a significant number of
517 data points distributed in each cluster. In this section we present the mean optical, chemical, and
518 microphysical properties for each cluster. The average properties are calculated for all data points
519 associated to the 6 individual clusters (all flights, both CONCERT campaigns). Figures 6a, 6c, and
520 6d show the normalized frequency distributions of the asymmetry parameter (gPN), the extinction
521 coefficient (ExtPN), and NO concentrations for the six clusters, respectively. Figure 6b represents the
522 mean normalized scattering phase functions of each clusters. However, it should be noted that the
523 number of data points could differ significantly from one cluster to another (from 141 measurements
524 for Cluster YC1 to 8950 measurements for Cluster AC1).

525 The asymmetry parameter gPN statistics shown in Fig. 6a provide the most striking evidence
526 of the relationship between contrail evolution stage and optical properties. In agreement with findings
527 of Gayet et al. (2012), aged contrails (cluster AC1 and AC2) and cirrus (cluster CC) correspond to
528 gPN values ranging from 0.72 to 0.80. Younger contrails (cluster YC1 and YC2) have values of gPN
529 of 0.80 to 0.86. Values of the asymmetry parameter in the primary wake (cluster PW) are typically
530 above 0.86. These features are a consequence of the time evolution of ice crystal shapes from quasi-
531 spherical ice particle after exhaust to non-spherical (e.g. column, needle, bullet, and bullet-rosette
532 type crystals) as the contrail evolves. In the primary wake, the pressure increases in the descending
533 vortex. This leads to adiabatic heating and subsequent sublimation of the ice crystals (Lewellen and
534 Lewellen, 2001; Unterstrasser et al., 2016) that can explain the spherical shapes of ice crystals and
535 thus, the high values of the asymmetry coefficients.

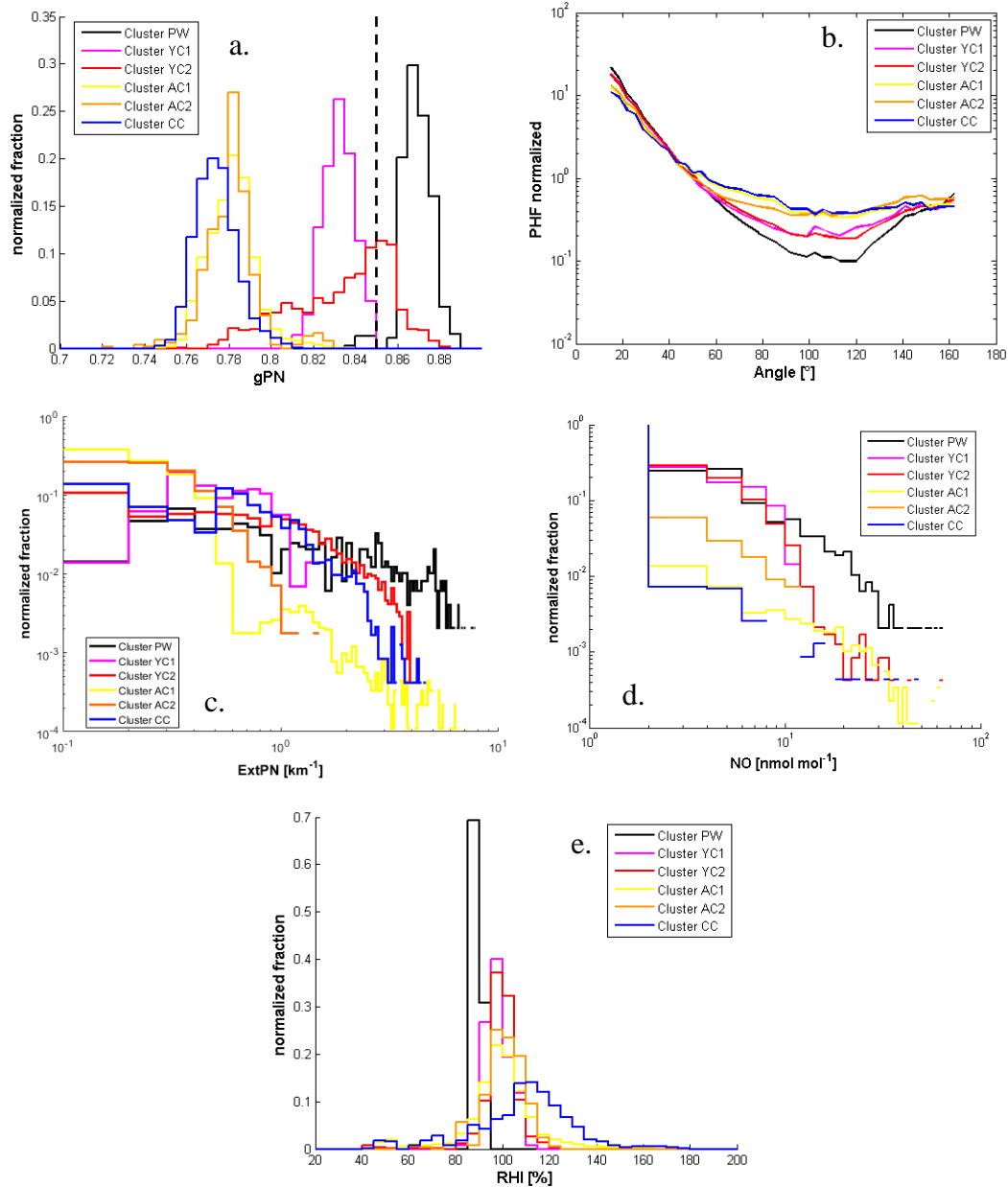


Figure 6: Normalized histograms of a) asymmetry coefficient (dashed line corresponds to a value of 0.85), b) phase function, c) extinction retrieved by Polar Nephelometer, d) NO concentration for all flights, and e) RHI conditions for CONCERT-2 flights.

536 The normalized phase functions are presented in Fig. 6b. Primary wake phase functions
 537 (cluster PW) are clearly different from the young contrail phase functions (cluster YC1 and YC2),
 538 which are themselves different from aged contrails (cluster AC1 and AC2) and cirrus (cluster CC)
 539 phase functions. The main difference is observed in the side scattering region (50°-140°). This region
 540 is related to changes of ice particles shapes and to the fraction of spherical ice crystals within the
 541 contrails. This behaviour is expected and agrees with the position of clusters PW, YC2 and YC1 on
 542 the expansion coefficient diagram (Fig. 2). Indeed, the decrease of the C_{j2} coefficient is associated to
 543 a side scattering enhancement. Therefore, very young contrails are composed mainly of spherical ice
 544 crystals for which the phase functions indicate a substantial scattering at forward angles and much
 545 lower scattering at sideward angles. As the contrails evolve, these features smooth out leading to
 546 phase functions with a featureless flat behaviour at side scattering angles. Finally, the averaged
 547 normalized phase functions of old contrails and cirrus are similar to each other. This also explains
 548 that they are difficult to discriminate within the PCA.

549 The extinction coefficient statistics are presented in Fig. 6c. All the aged contrails (cluster
550 AC1 and AC2) exhibit extinction coefficients lower than 2 km^{-1} . Also 80% of the sampled cirrus
551 (cluster CC) show such low extinction coefficients. For younger contrails (cluster YC1 and YC2), the
552 extinction coefficients can reach 5 km^{-1} . Largest extinction coefficients are found in primary wake
553 measurements (cluster PW) with values up to 8 km^{-1} . Still, the main fraction (more than 50% of data
554 points) of young contrail data yields extinction coefficients from 0 to 1 km^{-1} .

555 Concentrations of chemical species can also be used to characterize contrail/cirrus properties.
556 The concentration depends strongly on the type of the tracked aircraft. Figure 6d shows the mean
557 concentration of nitrogen oxide NO for the six individual clusters. Young contrail NO concentrations
558 (cluster PW, YC1 and YC2) can reach values up to 10 nmol mol^{-1} (corresponding to 10% of
559 measurements). For primary wake measurements (PW in black) a higher concentration can be
560 reached. Approximately 1% of the data have concentrations close to 60 nmol mol^{-1} in the primary
561 wake. In contrast, in aged contrails and in cirrus (cluster AC1, AC2 and CC) NO concentrations
562 higher than 2 nmol mol^{-1} do not exceed 1% of cases. Indeed, after exhaust, concentrations of nitrogen
563 oxide NO and sulphur dioxide SO₂ created by combustion reactions decrease rapidly due to the
564 dispersion in the upper troposphere and reactions with other molecules.

565 Due to high and similar nitrogen oxide concentrations in clusters AC1 and CC, we can
566 conclude that the clouds initially classified as “cirrus” are, in fact, significantly influenced by high-
567 density air traffic over Germany. In what follows, these parts of CONCERT measurements are
568 classified as “polluted cirrus” (cluster PC).

569 Finally, saturation conditions with respect to ice are presented in Fig. 6e for all clusters. The
570 predominant measured ambient relative humidity of all clusters is around 95%. Cluster AC1 and CC
571 (yellow and blue lines respectively) exhibit median RHI values close to 110% and 120% respectively.
572 These higher values are suitable for the persistence of the contrail and the formation of cirrus clouds
573 Supersaturated conditions are not reached for the measurements gathered in the primary wake cluster
574 (PW). Low humidity values may well occur in primary wakes with non-persisting contrails.

575 These results highlight that the principal component analysis, based on the ASC
576 measurements described in Sect. 3, can be used to discriminate contrail phases. Specific optical and
577 chemical properties can thus be derived for each contrail phase and can be related to their evolution.

578 **4.2 Microphysical cluster properties**

579 Microphysical properties are assessed using the combination of FSSP-300 and 2DC
580 measurements or hydrometeor diameters ranging from $0.5 \text{ }\mu\text{m}$ to $800 \text{ }\mu\text{m}$, but with a gap in the size
581 range $17 \text{ }\mu\text{m}$ to $50 \text{ }\mu\text{m}$. Figure 7 shows the averaged number particle size distributions (PSD) for each
582 cluster and for all flights of the study (8 flights from CONCERT-1 and 2). A linear interpolation in
583 logarithmic space is applied for each PSD to cover the gap from $17 \text{ }\mu\text{m}$ to $50 \text{ }\mu\text{m}$. Because of this
584 gap, the derived microphysical properties should be considered with caution, but may be used to
585 check the cluster definitions.

586 PSD measurements in natural cirrus and aged contrails differ significantly depending on the
587 location of the study, ambient air conditions, measurement methods (instrument limitation (Gayet et
588 al., 2002), and air speed (Febvre et al., 2009)). Previous studies show that a 3-hours old contrail cirrus
589 with an effective diameter close to $20 \text{ }\mu\text{m}$ (Voigt et al., 2017) and number concentration larger than
590 0.1 cm^{-3} (Schumann et al., 2017) can be composed of ice crystals with sizes up to $100 \text{ }\mu\text{m}$ (blue dashed
591 line, contrail cirrus figure 7). This differs from the PSD of the natural cirrus presented by Voigt et al.
592 (2017) (dashed black line), which has an order of magnitude lower particle number concentration. In

593 natural cirrus at mid-latitudes, ice crystals with size up to 1600 μm were observed during the ML-
 594 CIRRUS campaign (dark dashed line Figure 7, Voigt et al., 2017).

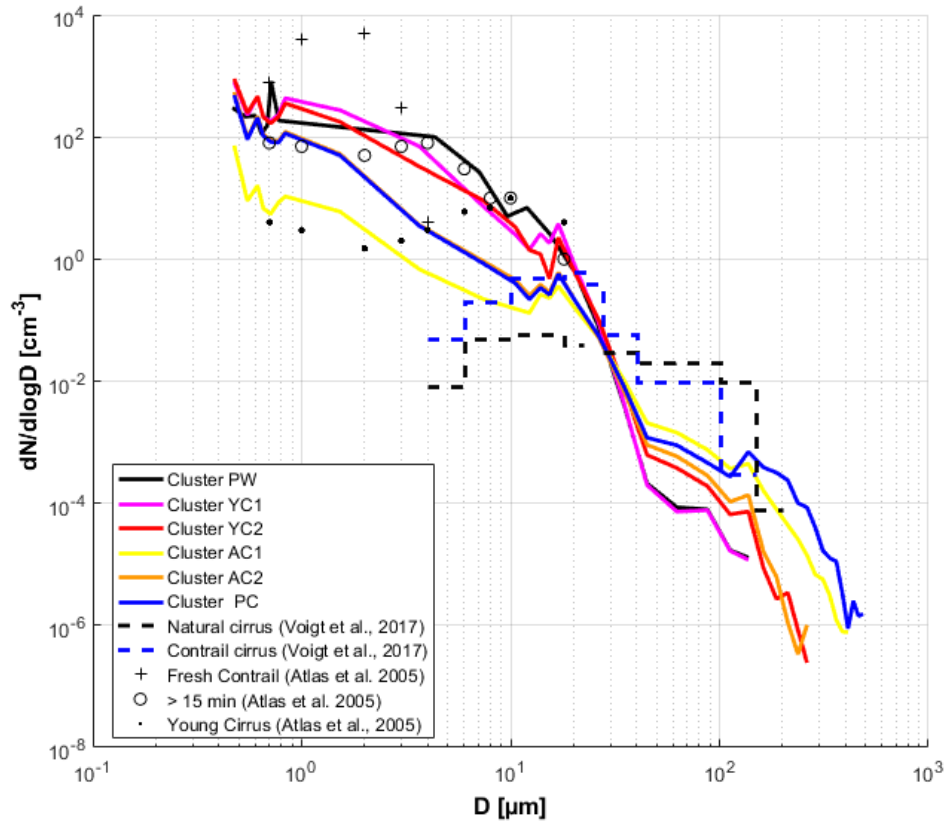


Figure 7: Number particle size distribution for each cluster including all data points of all flights. FSSP-300 measurements from 0.5 to 17 μm and 2DC measurements from 50 μm to 800 μm . The data are linearly interpolated in logarithm space between 17 μm and 50 μm .

595 Figure 7 shows that the mean number PSDs of each cluster are mainly consistent with the
 596 cluster definition and these previous studies. Indeed, two categories of PSD can be observed. Within
 597 the FSSP-300 size range, PSD relative to old contrails (cluster AC1 and AC2) and polluted cirrus
 598 (cluster PC) exhibit number concentration of small ice particles one order of magnitude lower than
 599 young contrails (clusters YC1 and YC2) and primary wake (cluster PW). Differences in this size
 600 range should be carefully considered due to uncertainties of the FSSP-300 number concentration
 601 measurements, which is close to 30% for typical concentrations of 5cm^{-3} but can reach 75% for
 602 concentrations of approximately 0.5cm^{-3} (Gayet et al., 2002). However, we can still discriminate
 603 primary wake measurements (cluster PW) from secondary wake measurements (clusters YC1 and
 604 YC2) in the 3 to 10 μm size range.

605 In addition, the differences observed between the PSD of PW/YC1/YC2 and AC1/AC2/PC
 606 can be explained by the production of small ice crystals (from 1 to 10 μm) in fresh exhaust plumes
 607 followed by rapid dilution during subsequent minutes after the exhaust. It is important to note that
 608 aged contrail measurements classified into the AC1 cluster present significantly lower ice particle
 609 concentrations than polluted cirrus. The small differences between the two clusters in optical and
 610 chemical properties may be, explained by strong shattering effects, as mentioned previously. Indeed,
 611 the shattering of large ice particles (diameters larger than 100 μm) can increase the particle number
 612 concentrations significantly (Febvre et al., 2009).

613 Even if though ice fragments from shattering influence ice particle concentrations in the 2DC size
 614 range, the PSDs are still consistent with the cluster definitions. A higher concentration of large ice
 615 crystals with diameters around 100 μm and larger are expected for cirrus (cluster PC) and for
 616 significantly well-developed contrails (cluster AC1 and AC2). This is particularly well illustrated by
 617 the mean PSD from cluster YC1 that displays significantly less particles in the 2DC measurements
 618 size range than the one corresponding to AC1 and AC2.

Extinction (km^{-1})		Mean	std	Mediane	prctile 25	prctile 75
cluster	PW	4,230	3,820	3,308	1,104	6,485
	YC1	0,720	0,410	0,680	0,351	1,026
	YC2	2,070	2,655	1,017	0,271	2,836
	AC1	0,220	0,484	0,037	0,008	0,158
	AC2	0,110	0,161	0,054	0,004	0,126
	PC	0,370	1,240	0,046	0,001	0,132

IWC (mg m^{-3})		Mean	std	Mediane	prctile 25	prctile 75
cluster	PW	8,173	10,586	5,573	1,665	11,363
	YC1	0,191	0,107	0,168	0,111	0,281
	YC2	4,860	8,918	1,235	0,218	6,604
	AC1	7,072	35,765	0,124	0,000	1,151
	AC2	0,295	1,079	0,094	0,003	0,286
	PC	27,929	144,384	0,126	0,005	0,448

NTOTAL (cm^{-3})		Mean	std	Mediane	prctile 25	prctile 75
cluster	PW	172,965	114,497	152,398	95,564	223,374
	YC1	409,726	205,625	405,127	230,907	603,187
	YC2	188,139	199,736	125,344	52,584	236,100
	AC1	8,206	6,550	1,696	0,966	3,363
	AC2	28,883	43,758	9,176	2,954	42,626
	PC	5,092	24,453	3,444	1,467	6,511

Table 3: Optical and microphysical properties for each cluster according interpolated particle size distributions from FSSP-300 and 2DC measurements.

619 Table 3 presents ice water content (IWC, in mg m^{-3}) and total number of ice crystals
 620 (NTOTAL, in cm^{-3}) derived from the measured PSD for each cluster. The extinction coefficient (in
 621 km^{-1}) obtained from the PN measurements is also displayed. Despite the large uncertainties associated
 622 to both instruments and the interpolation between 17 μm and 50 μm diameters, these results again
 623 show that each cluster can be connected to a specific contrail phase, and their properties can be
 624 compared to previous studies.

625 In terms of cluster mean values, the microphysical and optical properties of cluster PW agree
 626 with the cloud properties expected in the primary wakes. The extinction coefficient has a mean value
 627 of 4.23 km^{-1} , IWC is close to 28 mg m^{-3} , and the number concentration yields a typical value of 173
 628 particles cm^{-3} . These properties are in agreement with previous measurement reported by Gayet et al.
 629 (2012) with particle number concentrations close to 200 cm^{-3} for contrails less than 60 s after their
 630 formation. Their work also reports extinction coefficient around 7 km^{-1} presenting the highest values
 631 of the contrail life time.

632 Young (clusters YC1 and YC2) and aged contrails (clusters AC1 and AC2) exhibit distinctive
 633 differences in their extinction coefficients and their concentrations of ice particles. Higher extinction
 634 coefficients and ice number concentration, more than 0.7 km^{-1} and 170 cm^{-3} , respectively,
 635 characterize young contrails compared to aged contrails, with less than 0.4 km^{-1} and around 10

636 particles cm^{-3} , respectively. The ice number concentrations are in agreement with previous results
637 with values between 200 and 100 cm^{-3} for contrail ages between 60 s and 3 min, and around 5 cm^{-3}
638 for contrail ages around 10 min (Goodman et al., 1998 ; Lawson et al., 1998 ; Schröder et al., 2000 ;
639 Schäuble et al., 2009 ; Gayet et al., 2012 ; Voigt et al., 2017). The IWC values differ significantly
640 between clusters YC1 and YC2 which may be due to a lower number of large particles with diameter
641 higher than $20 \mu\text{m}$ in YC1 than in YC2.

642 Cluster PC corresponds to polluted cirrus. The IWC is significantly higher (28 mg m^{-3}) within
643 this cluster than in other clusters, and higher than observed in previous studies for clean natural cirrus.
644 Also, the ice number concentration and the extinction coefficient for cluster PC are higher than for
645 clean cirrus, with values around 0.1 cm^{-3} and 0.023 km^{-1} respectively. As mentioned in section 4.1,
646 cirrus observed during CONCERT campaigns are largely influenced by high-density air traffic over
647 Germany and it is thus still difficult to separate aged-contrails and natural cirrus based on their
648 scattering properties. In addition, shattering effects may have significantly influenced the number
649 concentrations of ice particle as discussed previously (section 2.2). Indeed, if only particles with
650 diameters larger than $50 \mu\text{m}$ are analysed, which better corresponds to an expected cirrus range, the
651 mean number concentration for the polluted cirrus cluster is 0.001 cm^{-3} .

652 **Conclusions**

653 In this study, a new form of statistical analysis of contrail to cirrus evolution is presented
654 based on two intensive contrail measurement campaigns, CONCERT-1 and CONCERT-2. The data
655 are used to study optical and microphysical properties of contrails during their evolution from young
656 contrails to contrail-cirrus clouds. The combination of optical, microphysical, chemical airborne
657 measurements with aircraft chasing information from ATC was used to provide an extended view of
658 cloud properties.

659 A Principal Component Analysis (PCA) methodology was applied to the measured Polar
660 Nephelometer scattering phase function data to facilitate the discrimination of cloud properties of
661 different contrail phases. The PCA results were derived first for two reference flights that sampled
662 contrails and cirrus in various development stages, including the primary wake, the young secondary
663 wake, old contrails (few minutes after formation) and polluted cirrus. For these flights, the PCA
664 clearly demonstrates its potential to discriminate different groups of clouds, justifying the use of these
665 two flights as a benchmark. Thereafter, the scattering phase functions measured during other
666 CONCERT flights were projected into the space of principal components obtained from the two
667 reference flights. Individual data points were assigned to the predefined cluster with minimum
668 Mahalanobis distances. From the entire data set, the cloud properties in the various contrail
669 development stages can be analysed separately.

670 The analysis demonstrates that the clearest separation between clusters is derived from
671 particle shape, which impacts the scattering phase function and the derived asymmetry parameter
672 gPN. The asymmetry parameter clearly separates young contrails (gPN of 0.72 to 0.80) from
673 contrail/cirrus with gPN ranging from 0.80 to 0.88. Since the exact contrail age was not always
674 known, young and aged contrails are classified also by their optical and chemical properties. The
675 measured NO concentrations are also useful to distinguish cirrus from old contrails. However, no
676 strictly clean cirrus has been observed during these two campaigns due to strong influence from dense
677 air traffic over Germany.

678 Despite the large size gap between the size ranges of the two instruments used, particle size
679 spectra and related mean values of the ice particle number concentration, extinction and ice water
680 content have been determined for each cluster. The various clusters clearly show different size

681 distributions. In good agreement with previous findings on optical and chemical properties, we find
682 that young contrails have more than a factor of ten higher number concentrations of small ice crystals
683 (with diameters lower than 20 μm) than aged contrails. On the other hand, aged contrails and polluted
684 cirrus contain larger ice crystals, with diameters larger than 75 μm . The optical and microphysical
685 properties of the aged contrail cirrus are often similar to those found in the polluted cirrus clouds. The
686 results show that the PCA method allows to identify and discriminate different contrail growth stages
687 and to provide an independent method for the characterization of the evolution of contrail properties.

688 In agreement with Shcherbakov et al. (2016), who characterised volcanic and cirrus using
689 optical measurements, the PCA method has been clearly shown here to be suitable for contrail studies.
690 The additional use of microphysical and chemical measurements can be added to the PCA method in
691 order to improve the selection of contrail phases. Different ranges of extinction or asymmetric
692 coefficients could be also used for PCA analyses in this perspective. However, additional parameters
693 should be carefully selected to limit the bias introduced by the limitations of the probes and the
694 optimal selection may vary from one measurement campaign to another.

695 Accurate modelling of cirrus or contrails' single scattering properties is required for the
696 interpretation of remote sensing measurements. Therefore, measurements of the optical
697 characteristics of ice crystals in natural conditions are still needed for validation of numerical
698 techniques and for the determination of free parameters in light scattering models. In this context, the
699 results from the PCA could be used to develop representative parameterizations of the scattering
700 properties and the ice crystals' shapes and sizes observed in the visible wavelength range.

701 **Acknowledgments**

702 We thank for financial support by the Helmholtz Association under contract VH-NG-309 and
703 W2/W3-60. Part of this work was funded by DFG SPP HALO 1294 contract VO1504/4-1, and by the
704 DLR project Eco2Fly in ML-CIRRUS-cirrus special issue. We thank Lufthansa, the DLR flight
705 department and the Deutsche Flugsicherung for excellent support during the campaign. The in-situ
706 data can be found in the HALO-database (<https://halo-db.pa.op.dlr.de/>).

707 **References**

- 708 Baran, A.J., Gayet, J.-F., and Shcherbakov, V.: On the interpretation of an unusual in-situ measured
709 ice crystal scattering phase function. *Atmospheric Chemistry and Physics* 12, 9355–9364, 2012.
- 710
- 711 Baumgardner, D., Dye, J.E., Gandrud, B.W., and Knollenberg, R.G.: Interpretation of measurements
712 made by the forward scattering spectrometer probe (FSSP-300) during the Airborne Arctic
713 Stratospheric Expedition. *Journal of Geophysical Research* 97, 8035–8046, 1992.
- 714
- 715 Borrmann, S., Luo, B., and Mishchenko, M.: Application of the T-Matrix Method to the Measurement
716 of Aspherical (Ellipsoidal) Particles with Forward Scattering Optical Particle Counters. *Journal of*
717 *Aerosol Science* 31, no. 7 (2000): 789–799, 2000.
- 718
- 719 Burkhardt, U., Kärcher, B., and Schumann, U.: Global modeling of the contrail and contrail cirrus
720 climate impact. *Bulletin of the American Meteorological Society* 91, 479–484, 2010.
- 721
- 722 Burkhardt, U. and Kärcher, B.: Global radiative forcing from contrail cirrus. *Nature Climate Change*,
723 1(1), 54–58, 2011.
- 724

725 Carleton, A.M., Silva, A.D., Aghazarian, M.S., Bernhardt, J., Travis, D.J., and Allard, J.: Mid-season
726 climate diagnostics of jet contrail “outbreaks” and implications for eastern US sky-cover trends.
727 *Climate Research*, 56, 209–230, 2013.
728

729 Chen, C.-C. and Gettelman, A.: Simulated 2050 aviation radiative forcing from contrails and aerosols.
730 *Atmospheric Chemistry and Physics*, 16(11), 7317–7333, 2016.
731

732 Duda, D. P., Minnis, P., Khlopenkov, K., Chee, T.L., and Boeke, R.: Estimation of 2006 Northern
733 Hemisphere Contrail Coverage Using MODIS Data. *Geophysical Research Letters*, 40, 612-617,
734 doi:10.1002/grl.50097, 2013.
735

736 Febvre, G., Gayet, J.-F., Minikin, A., Schlager, H., Shcherbakov, V., Jourdan, O., Busen, R., Fiebig,
737 M., Kärcher, B., and Schumann, U.: On optical and microphysical characteristics of contrails and
738 cirrus. *Journal of Geophysical Research: Atmospheres* (1984–2012) 114, 2009.
739

740 Frömming, C., Ponater, M., Dahlmann, K., Grewe, V., Lee, D.S., and Sausen, R.: Aviation-induced
741 radiative forcing and surface temperature change in dependency of the emission altitude. *Journal*
742 *of Geophysical Research: Atmospheres* (1984–2012) 117, 2012.
743

744 Gayet, J.F., Crépel, O., Fournol, J.F., and Oshchepkov, S.: A new airborne Polar Nephelometer for
745 the measurements of optical and microphysical cloud properties. Part I: Theoretical design. In
746 *Annales Geophysicae*, pp. 451–459, 1997.
747

748 Gayet, J.-F., Auriol, F., Minikin, A., Ström, J., Seifert, M., Krejci, R., Petzold, A., Febvre, G., and
749 Schumann, U.: Quantitative Measurement of the Microphysical and Optical Properties of Cirrus
750 Clouds with Four Different in Situ Probes: Evidence of Small Ice Crystals. *Geophysical Research*
751 *Letters* 29, no. 24: 2230. doi:10.1029/2001GL014342, 2002.
752

753 Gayet, J.-F., Ovarlez J., Shcherbakov, V., Ström, J., Schumann, U., Minikin, A., Auriol, F., Petzold,
754 A., and Monier M.: Cirrus Cloud Microphysical and Optical Properties at Southern and Northern
755 Midlatitudes during the INCA Experiment. *Journal of Geophysical Research: Atmospheres* 109,
756 no. D20 : D20206. doi:10.1029/2004JD004803, 2004.
757

758 Gayet, J.-F., Shcherbakov, V., Voigt, C., Schumann, U., Schäuble, D., Jeßberger, P., Petzold, A.,
759 Minikin, A., Schlager, H., Dubovik, O., and Lapyonok, T.: The evolution of microphysical and
760 optical properties of an A380 contrail in the vortex phase. *Atmospheric Chemistry and Physics*. 12,
761 6629–6643, 2012.
762

763 Garrett, T.J., Gerber, H., Baumgardner, D.G., Twohy, C.H., and Weinstock, E.M.: Small, highly
764 reflective ice crystals in low-latitude cirrus. *Geophysical Research Letters* 30, 2132, 2003.
765

766 Gettelman, A., and Chen, C.: The climate impact of aviation aerosols. *Geophysical Research Letters*,
767 40, 2785–2789, doi:10.1002/grl.50520, 2013.
768

769 Gierens, K. and Dilger, F.: A climatology of formation conditions for aerodynamic contrails,
770 *Atmospheric Chemistry and Physics*, 13, 10847-10857, doi:10.5194/acp-13-10847-2013, 2013.
771

772 Graf, K., Schumann, U., Mannstein, H., and Mayer, B.: Aviation induced diurnal North Atlantic cirrus
773 cover cycle. *Geophysical Research Letters* 39, L16804, doi:10.1029/2012GL052590, 2012.
774

775 Goodman, J., Pueschel, R.F., Jensen, E.J., Verma, S., Ferry, G.V., Howard, S.D., Kinne, S.A., and
776 Baumgardner, D.: Shape and size of contrails ice particles. *Geophysical Research Letters* 25, 1327–
777 1330, 1998.

778

779 Heller, R., Voigt, C., Beaton, S., Dörnbrack, A., Kaufmann, S., Schlager, H., Wagner, J., Young, K.,
780 and Rapp, M.: Mountain waves modulate the water vapor distribution in the UTLS, *Atmospheric*
781 *Chemistry and Physics, Discussion*, doi:10.5194/acp-2017-334, in review.

782

783 Heymsfield, A.J., and Parrish, J.L.: A computational technique for increasing the effective sampling
784 volume of the PMS two-dimensional particle size spectrometer. *Journal of Applied Meteorology*
785 17, 1566–1572, 1978.

786 Heymsfield, A., Baumgardner, D., DeMott, P., Forster, P., Gierens, K., and Kärcher, B.: Contrail
787 Microphysics. *Bulletin of the American Meteorological Society* 91, 465–472, 2010.

788

789 Irvine, E.A., Hoskins, B.J., and Shine, K.P.: The dependence of contrail formation on the weather
790 pattern and altitude in the North Atlantic. *Geophysical Research Letters* 39, L12802,
791 doi:10.1029/2012GL051909, 2012.

792

793 Järvinen, E., Schnaiter, M., Mioche, G., Jourdan, O., Shcherbakov, V.N., Costa, A., Afchine, A.,
794 Krämer, M., Heidelberg, F., Jurkat, T., Voigt, C., Schlager, H., Nichman, L., Gallagher, M., Hirst,
795 E., Schmitt, C., Bansemer, A., Heymsfield, A., Lawson, P., Tricoli, U., Pfeilsticker, K., Vochezer,
796 P., Möhler, O., and Leisner, T.: Quasi-spherical Ice in Convective Clouds, *Journal of Atmospheric*
797 *Sciences*, doi:10.1175/JAS-D-15-0365.1, 2016.

798

799 Jansen, J. and Heymsfield, A. J.: Microphysics of aerodynamic contrail formation processes, *Journal*
800 *of Atmospheric Sciences*, 72(9), 3293–3308, 2015.

801

802 Jeßberger, P., Voigt, C., Schumann, U., Sölch, I., Schlager, H., Kaufmann, S., Petzold, A., Schäuble,
803 D., and Gayet, J.F.: Aircraft type influence on contrail properties, *Atmospheric Chemistry and*
804 *Physics*, 13, 11965-11984, doi:10.5194/acp-13-11965-2013, 2013.

805

806 Jourdan, O., Oshchepkov, S., Gayet, J.-F., Shcherbakov, V., and Isaka, H.: Statistical analysis of
807 cloud light scattering and microphysical properties obtained from airborne measurements. *Journal*
808 *of Geophysical Research* 108, 4155, 2003.

809

810 Jourdan, O., Mioche, G., Garrett, T.J., Schwarzenböck, A., Vidot, J., Xie, Y., Shcherbakov, V., Yang,
811 P., and Gayet, J.-F.: Coupling of the microphysical and optical properties of an Arctic nimbostratus
812 cloud during the ASTAR 2004 experiment: Implications for light-scattering modeling. *Journal of*
813 *Geophysical Research: Atmospheres* (1984–2012) 115, 2010.

814

815 Jurkat, T., Voigt, C., Arnold, F., Schlager, H., Aufmhoff, H., Schmale, J., Schneider, J., Lichtenstern,
816 M., and Dörnbrack, A.: Airborne stratospheric ITCIMS-measurements of SO₂, HCl, and HNO₃ in
817 the aged plume of volcano Kasatochi, *Journal of Geophysical Research*, 115, D00L17,
818 doi:10.1029/2010JD013890, 2010.

819

820 Jurkat, T., Voigt, C., Arnold, F., Schlager, H., Kleffmann, J., Aufmhoff, H., Schäuble, D., Schäfer,
821 M., and Schumann, U.: Measurements of HONO, NO, NO_y and SO₂ in aircraft exhaust plumes at
822 cruise, *Geophysical Research Letters*, 38, L10807, doi:10.1029/2011GL046884, 2011.

823

824 Jurkat, T., Kaufmann, S., Voigt, C., Schäuble, D., Jeßberger, P., and Ziereis, H.: The airborne mass
825 spectrometer AIMS – Part 2: Measurements of trace gases with stratospheric or tropospheric origin
826 in the UTLS, *Atmospheric Measurement Technics*, 9, 1907–1923, doi:10.5194/amt-9-1907-2016,
827 2016.

828

829 Kärcher, B., and Voigt, C.: Formation of nitric acid/water ice particles in cirrus clouds, *Geophysical*
830 *Research Letters*, 33, L08806, doi:10.1029/2006GL025927, 2006.

831

832 Kärcher, B., and Voigt, C.: Susceptibility of contrail ice crystal numbers to aircraft soot particle
833 emissions, *Geophysical Research Letters*, 44, 8037-8046, doi:10.1002/2017GL074949, 2017.

834

835 Kärcher, B., and Yu, F.: Role of aircraft soot emissions in contrail formation. *Geophysical Research*
836 *Letters*, 36, L01804, doi:10.1029/2008GL036649, 2009.

837

838 Kaufmann, S., Voigt, C., Jeßberger, P., Jurkat, T., Schlager, H., Schwarzenboeck, A., Klingebiel, M.,
839 and Thornberry, T.: In situ measurements of ice saturation in young contrails, *Geophysical*
840 *Research Letters*, 41, doi:10.1002/2013GL058276, 2014.

841

842 Kaufmann, S., Voigt, C., Jurkat, T., Thornberry, T., Fahey, D. W., Gao, R.-S., Schlage, R., Schäuble,
843 D., and Zöger, M.: The airborne mass spectrometer AIMS – Part 1: AIMS-H₂O for UTLS water
844 vapor measurements, *Atmospheric Measurement Technics*, 9, 939-953, doi:10.5194/amt-9-939-
845 2016, 2016.

846

847 Kübbeler, M., Hildebrandt, M., Meyer, J., Schiller, C., Hamburger, Th., Jurkat, T., Minikin, A.,
848 Petzold, A., Rautenhaus, M., Schlager, H., Schumann, U., Voigt, C., Spichtinger, P., Gayet, J.-F.,
849 Goubeyre, C., and Krämer, M.: Thin and subvisible cirrus and contrails in a subsaturated
850 environment, *Atmospheric Chemistry and Physics*, 11, 5853-5865, doi:10.5194/acp-11-5853-
851 2011, 2011.

852

853 Lawson, R. Paul, Andrew J. Heymsfield, Steven M. Aulenbach, et Tara L. Jensen. « Shapes, sizes
854 and light scattering properties of ice crystals in cirrus and a persistent contrail during SUCCESS ». *Geophysical research letters* 25, no 9: 1331–1334, 1998.

855

856

857 Lawson, R.P., O’Connor, D., Zmarzly, P., Weaver, K., Baker, B., Mo, Q., and Jonsson, H.: The 2D-
858 S (stereo) probe: Design and preliminary tests of a new airborne, high-speed, high-resolution
859 particle imaging probe. *Journal of Atmospheric and Oceanic Technology* 23, 1462–1477, 2006.

860

861 Lee, D.S., Pitari, G., Grewe, V., Gierens, K., Penner, J.E., Petzold, A., Prather, M.J., Schumann, U.,
862 Bais, A., and Bernsten, T.: Transport impacts on atmosphere and climate: Aviation. *Atmospheric*
863 *Environment* 44, 4678–4734, 2010.

864

865 Legendre, P., and Legendre, L.: *Numerical Ecology*, 2nd English ed., 853 pp., Elsevier Science, New
866 York, 1998.

867

868 De León, R.R., Krämer, M., Lee, D.S., and Thelen, J.C.: Sensitivity of radiative properties of
869 persistent contrails to the ice water path. *Atmospheric Chemistry and Physics*. 12, 7893–7901,
870 2012.

871

872 Lewellen, D.C.: Analytic solutions for evolving size distributions of spherical crystals or droplets
873 undergoing diffusional growth in different regimes. *Journal of the Atmospheric Sciences* 69, 417–
874 434, 2012.

875

876 Lewellen, D.C., and Lewellen, W.S.: The effects of aircraft wake dynamics on contrail development.
877 *Journal of the Atmospheric Sciences* 58, 390–406, 2001.

878

879 Liou, K.N., Takano, Y., Yue, Q., and Yang, P.: On the radiative forcing of contrail cirrus
880 contaminated by black carbon. *Geophysical Research Letters*, 40, 778–784, doi:10.1002/grl.50110,
881 2013.

882

883 De Maesschalck, R., Jouan-Rimbaud, D., and Massart, D.L.: The Mahalanobis Distance.
884 *Chemometrics and Intelligent Laboratory Systems* 50, no. 1: 1–18. doi:10.1016/S0169-
885 7439(99)00047-7, 2010.

886

887 Meyer, J., Rolf, C., Schiller, C., Rohs, S., Spelten, N., Afchine, A., Zöger, M., Sitnikov, N.,
888 Thornberry, T. D., Rollins, A. W., Bozóki, Z., Tátrai, D., Ebert, V., Kühnreich, B., Mackrodt, P.,
889 Möhler, O., Saathoff, H., Rosenlof, K. H., and Krämer, M.: Two decades of water vapor
890 measurements with the FISH fluorescence hygrometer: a review, *Atmospheric Chemistry and*
891 *Physics*, 15, 8521–8538, doi:10.5194/acp-15-8521-2015, 2015.

892

893 Mishchenko, M.I., Travis, L.D., Kahn, R.A., and West, R.A.: Modeling phase functions for dustlike
894 tropospheric aerosols using a shape mixture of randomly oriented polydisperse spheroids. *Journal*
895 *of Geophysical Research* 102, 16831–16, 1997.

896

897 Moore, R. H., Thornhill, K. L., Weinzierl, B., Sauer, D., D’Ascoli, E., Kim, J., Lichtenstern, M.,
898 Scheibe, M., Beaton, B., Beyersdorf, A. J., Barrick, J., Bulzan, D., Corr, C. A., Crosbie, E., Jurkat,
899 T., Martin, R., Riddick, D., Shook, M., Slover, G., Voigt, C., White, R., Winstead, E., Yasky, R.,
900 Ziemba, L. D., Brown, A., Schlager, H., and Anderson, B. E.: Biofuel blending reduces particle
901 emissions from aircraft engines at cruise conditions, *Nature*, 543, 411-415, 10.1038/nature21420,
902 2017.

903

904 Schäuble, D., Voigt, C., Kärcher, B., Stock, P., Schlager, H., Krämer, M., Schiller, C., Bauer, R.,
905 Spelten, N., De Reus, M., Szakáll, M., Borrmann, S., Weers, U., and Peter T.: Airborne
906 measurements of the nitric acid partitioning in persistent contrails, *Atmospheric Chemistry and*
907 *Physics*, 9, 8189-8197, 2009.

908

909 Schlager, H., Konopka, P., Schulte, P., Schumann, U., Ziereis, H., Arnold, F., Klemm, M., Hagen,
910 D.E., Whitefield, P.D., and Ovarlez, J.: In situ observations of air traffic emission signatures in the
911 North Atlantic flight corridor. *Journal of Geophysical Research* 102, 10739–10, 1997.

912

913 Schröder, F., Kärcher, B., Duroure, C., Ström, J., Petzold, A., Gayet, J.-F., Strauss, B., Wendling, P.,
914 and Borrmann, S.: On the Transition of Contrails into Cirrus Clouds. *Journal of the Atmospheric*
915 *Sciences* 57, 464–480, 2000.

916

917 Schumann, U.: On conditions for contrail formation from aircraft exhausts. *Meteorologische*
918 *Zeitschrift*, 5, 4–23, 1996.

919

920 Schumann, U., and Heymsfield, A.: On the lifecycle of individual contrails and contrail cirrus,
921 Meteorological Monographs, 58, 3.1-3.24, doi: 10.1175/AMSMONOGRAPHS-D-16-0005.1,
922 2017.

923

924 Schumann, U., Jeßberger, P., and Voigt, C.: Contrail ice particles in aircraft wakes and their climatic
925 importance, Geophysical Research Letters, 40, 2867-2872, doi: 10.1002/grl.50539, 2013.

926

927 Schumann, U., Mayer, B., Gierens, K., Unterstrasser, S., Jessberger, P., Petzold, A., Voigt, C., and
928 Gayet, J.-F.: Effective Radius of Ice Particles in Cirrus and Contrails. Journal of the Atmospheric
929 Sciences, 68, 300–321, 2011.

930

931 Schumann, U., Penner, J.E., Chen, Y., Zhou, C., and Graf, K.: Dehydration effects from contrails in
932 a coupled contrail-climate model, Atmospheric Chemistry and Physics, 15, 11179-11199, doi:
933 10.5194/acp-15-11179-2015, 2015.

934

935 Schumann, U., Kiemle, C., Schlager, H., Weigel, R., Borrmann, S., D'Amato, F., Krämer, M.,
936 Matthey, R., Protat, A., Voigt, C., and Volk, C. M.: Long-lived contrails and convective cirrus
937 above the tropical tropopause, Atmospheric Chemistry and Physics, 17, 2311-2346,
938 doi:10.5194/acp-17-2311-2017, 2017a.

939

940 Schumann, U., Baumann, R., Baumgardner, D., Bedka, S. T., Duda, D. P., Freudenthaler, V., Gayet,
941 J.-F., Heymsfield, A. J., Minnis, P., Quante, M., Raschke, E., Schlager, H., Vázquez-Navarro, M.,
942 Voigt, C. and Wang, Z.: Properties of individual contrails: a compilation of observations and some
943 comparisons, Atmospheric Chemistry and Physics, 17(1), 403–438, doi:10.5194/acp-17-403-2017,
944 2017b.

945

946 Seber, G. A. F.: Multivariate analysis of variance and covariance. Multivariate observations, 433–
947 495, 1984.

948

949 Shcherbakov, V., Jourdan, O., Voigt, C., Gayet, J.F., Chauvigne, A., Schwarzenboeck, A., Minikin,
950 A., Klingebiel, M., Weigel, R., Borrmann, S., Jurkat, T., Kaufmann, S., Schlage, R., Gorbeyre,
951 C., Febvre, G., Lapyonok, T., Frey, W., Molleker, S., and Weinzierl, B.: Porous Aerosol in
952 Degassing Plumes of Mt. Etna and Mt. Stromboli. Atmospheric Chemistry Physics 16, no. 18:
953 11883–97. doi:10.5194/acp-16-11883-2016, 2016.

954

955 Spath, Helmuth. The Cluster Dissection and Analysis Theory FORTRAN Programs Examples.
956 Prentice-Hall, Inc., 1985.

957

958 Sussmann, R., and Gierens, K.M.: Lidar and numerical studies on the different evolution of vortex
959 pair and secondary wake in young contrails. Journal of Geophysical Research: Atmospheres 104,
960 2131–2142, 1999.

961

962 Sussmann, R., and Gierens, K.M.: Differences in early contrail evolution of two-engine versus four-
963 engine aircraft: Lidar measurements and numerical simulations. Journal of Geophysical Research:
964 Atmospheres 106, 4899–4911, 2001.

965

966 Vazquez-Navarro, M., Mannstein, H. and Kox, S.: Contrail life cycle and properties from 1 year of
967 MSG/SEVIRI rapid-scan images, Atmospheric Chemistry and Physics, 15(15), 8739–8749, 2015.

968

- 969 Voigt C., Schlager, H., Ziereis, H., Kärcher, B., Luo, B.P., Schiller, C., Krämer, M., Popp, P.J., Irie,
970 H., and Kondo, Y.: Nitric acid in cirrus clouds, *Geophysical Research Letters*, 33, L05803,
971 doi:10.1029/2005GL025159, 2006.
- 972
- 973 Voigt, C., Schumann, U., Jurkat, T., Schäuble, D., Schlager, H., Petzold, A., Gayet, J.-F., Krämer,
974 M., Schneider, J., Borrmann, S., Schmale, J., Jessberger, P., Hamburger, T., Lichtenstern, M.,
975 Scheibe, M., Gourbeyre, C., Meyer, J., Kübbeler, M., Frey, W., Kalesse, H., Butler, T., Lawrence,
976 M.G., Holzäpfel, F., Arnold, F., Wendisch, M., Döpelheuer, A., Gottschaldt, K., Baumann, R.,
977 Zöger, M., Sölch, I., Rautenhaus, M., and Dörnbrack, A.: In-situ observations of young contrails -
978 Overview and selected case studies from the CONCERT campaign, *Atmospheric Chemistry and
979 Physics*, 10, 9039–9056, doi:10.5194/acp-10-9039-2010, 2010.
- 980
- 981 Voigt, C., Schumann, U., Jessberger, P., Jurkat, T., Petzold, A., Gayet, J.-F., Krämer, M., Thornberry,
982 T., and Fahey, D.: Extinction and optical depth of contrails, *Geophysical Research Letters*, 38,
983 L11806, doi:10.1029/2011GL04718, 2011.
- 984
- 985 Voigt, C., Jessberger, P., Jurkat, T., Kaufmann, S., Baumann, R., Schlager, H., Bobrowski, N.,
986 Giuffrida, G., and Salerno, G.: Evolution of CO₂, SO₂, HCl, and HNO₃ in the Volcanic Plumes
987 from Etna. *Geophysical Research Letters*, 41, 6, 2196–2203. doi:10.1002/2013GL058974, 2014.
- 988
- 989 Voigt, C., Schumann, U., Minikin, A., Abdelmonem, A., Afchine, A., Borrmann, S., Boettcher, M.,
990 Buchholz, B., Bugliaro, L., Costa, A., Curtius, J., Dollner, M., Dörnbrack, A., Dreiling, V., Ebert,
991 V., Ehrlich, A., Fix, A., Forster, L., Frank, F., Fütterer, D., Giez, A., Graf, K., Groß, J.-U., Groß,
992 S., Heimerl, K., Heinold, B., Hüneke, T., Järvinen, E., Jurkat, T., Kaufmann, S., Kenntner, M.,
993 Klingebiel, M., Klimach, T., Kohl, R., Krämer, M., Krisna, T. C., Luebke, A., Mayer, B., Mertes,
994 S., Molleker, S., Petzold, A., Pfeilsticker, K., Port, M., Rapp, M., Reutter, P., Rolf, C., Rose, D.,
995 Sauer, D., Schäfler, A., Schlage, R., Schnaiter, M., Schneider, J., Spelten, N., Spichtinger, P.,
996 Stock, P., Walser, A., Weigel, R., Weinzierl, B., Wendisch, M., Werner, F., Wernli, H., Wirth, M.,
997 Zahn, A., Ziereis, H., and Zöger, M.: ML-CIRRUS - The airborne experiment on natural cirrus and
998 contrail cirrus with the high-altitude long-range research aircraft HALO, *Bulletin of the American
999 Meteorological Society*, doi: 10.1175/BAMS-D-15-00213, 2017.
- 1000
- 1001 Xie, Y., Yang, P., Gao, B.-C., Kattawar, G.W., and Mishchenko, M.I.: Effect of ice crystal shape and
1002 effective size on snow bidirectional reflectance. *Journal of Quantitative Spectroscopy and
1003 Radiative Transfer* 100, 457–469, 2006.
- 1004
- 1005 Xie, Y., Yang, P., Kattawar, G.W., Minnis, P., and Hu, Y.X.: Effect of the inhomogeneity of ice
1006 crystals on retrieving ice cloud optical thickness and effective particle size. *Journal of Geophysical
1007 Research: Atmospheres* (1984–2012) 114, 2009.
- 1008
- 1009 Yang, P., Hong, G., Dessler, A.E., Ou, S.S., Liou, K.-N., and Minnis, P.: Contrails and induced cirrus:
1010 Optics and radiation. *Bulletin of the American Meteorological Society* 91, 473–478, 2010.
- 1011
- 1012 Ziereis, H., Schlager, H., Schulte, P., Velthoven, P. van, and Slemr, F.: Distributions of NO, NO_x,
1013 and NO_y in the upper troposphere and lower stratosphere between 28 and 61 N during POLINAT
1014 2. *Journal of Geophysical Research: Atmospheres* (1984–2012) 105, 3653–3664, 2000.
- 1015
- 1016 Zöger, M., Afchine, A., Eicke, N., Gerhards, M-T., Klein, E., McKenna, D.S., Mörschel, U., Schmidt,
1017 U., Tan, V., Tuitjer, F., Woyke, T., Schiller, C. : Fast in situ stratospheric hygrometers: A new

1018 family of balloon-borne and airborne Lyman alpha photofragment fluorescence hygrometers.
1019 Journal of Geophysical Research: Atmospheres, 104, 1807-1816, 1999.
1020